

HUMBOLDT UNIVERSITÄT ZU BERLIN

MASTER'S THESIS

**Improvement of light yield and spatial resolution
of a liquid-scintillator detector equipped with a
wavelength-shifting optical module coupled to a
SiPM array**

Author:

Alexander VAGTS

Supervisor:

Prof. Dr. Heiko LACKER

Experimental Particle Physics 2 Group
Handed in to the Institut für Physik

4th July 2022

HUMBOLDT UNIVERSITÄT ZU BERLIN

Abstract

Mathematisch-Naturwissenschaftliche Fakultät
Institut für Physik

Master of Science

Improvement of light yield and spatial resolution of a liquid-scintillator detector equipped with a wavelength-shifting optical module coupled to a SiPM array

by Alexander VAGTS

This thesis was written in the framework of the planned Search for Hidden Particles (SHiP) experiment, an experiment looking for hidden sector particles and light dark matter. SHiP is designed to be a zero-background experiment. As an important component of background events consists of muons that enter the decay volume and deep inelastic neutrino scattering processes in the walls of the decay volume, an effective way to tag both kinds of background is needed. This is provided by the Surrounding Background Tagger (SBT), which will consist of several single cells filled with liquid scintillator. These scintillator boxes will be equipped with wavelength-shifting optical modules (WOMs) viewed by silicone photo-multiplier (SiPM) arrays.

The goal of this work was to contribute to the improvement of the efficiency of the background tagging.

It is studied whether the light yield of the liquid scintillator setup can be improved when a reflector is glued to the end of a WOM tube. Although the results remain inconclusive, an upper limit of 15 % can be established on the increase in light yield using a reflector.

Directional information is reconstructed from the light detected by the SiPM array, continuing studies presented in [10]. For a single event, it is possible to determine on which side of the PCB the light was created on a 2σ -level.

Acknowledgements

I would like to thank Prof. Dr. Heiko Lacker for his ongoing support, the great supervision and the opportunity to work in his sympathetic work group. Thanks to Dr. Christian Scharf for always helping and discussing problems whenever it was needed. Also thanks to my wonderful girlfriend Elisa Böhme for her support and her help.

Contents

Abstract	iii
1 Introduction	1
2 SHiP Experiment	5
3 Scintillation-based detection mechanisms	9
3.1 Scintillators	9
3.1.1 Liquid scintillators	11
3.1.2 Plastic scintillators	12
3.2 Wavelength-shifting optical modules	12
3.3 Silicon photo-multipliers	16
4 Cosmics setup and SiPM calibration setup	21
4.1 Readout hardware	21
4.1.1 SiPMs and PCBs	21
4.1.2 eMUSIC-Board	21
Changing the settings of the eMUSIC board	23
4.1.3 WaveCatcher	23
4.2 Cosmics setup	25
4.3 SiPM calibration setup	29
4.4 Dark counts, crosstalk and afterpulses	30
5 Data analysis, calibration and light yield comparison	33
5.1 Event properties	33
5.1.1 Signal shape of a SPAD	33
5.1.2 Signal shape of a SiPM	34
5.1.3 Noise and electronic influences	35
5.2 Conversion from raw data to .root file	38
5.2.1 RootReader	39
5.2.2 WaveCatcher Analysis	39
5.3 Baseline determination	40
5.3.1 RootReader	40

5.3.2	WaveCatcher Analysis	41
5.4	Integration window determination	43
5.4.1	RootReader	43
5.5	Charge and gain	44
5.6	The pulse-charge spectrum	46
5.6.1	Calibration value Λ_{pixel}	47
5.6.2	Light yield	47
5.7	Fitting of the pulse-charge spectrum	47
5.7.1	RootReader	47
Calibration measurements	48	
Cosmics measurements	48	
5.7.2	Motivation for the WaveCatcher Analysis	49
6	Light yield comparison	53
6.1	Breakdown voltage	53
6.2	Calibration results	54
6.2.1	Temperature dependence	55
6.3	Light yield comparison between the PCBs	56
6.4	Light yield with and without reflector	57
6.5	Light yield with and without black foil at the end of the WOM tube	61
7	Reconstruction of the azimuth angle of a particle	65
7.1	Incidence position of muons	65
7.1.1	Time resolution of the plastic scintillators	67
7.2	Azimuth angle of a charged particle using the PCB	70
7.2.1	Correction of the ϕ_{ew} value	72
7.2.2	Event-independent mean angle $\overline{\phi_{ew}}$	72
7.3	Directional reconstruction	73
8	Summary and outlook	77
A	Temperature dependence	81
B	Light yield comparison with and without reflector	83
C	Light yield comparison with and without black foil	87
D	PCB design	89
	Bibliography	91

List of Abbreviations

AP	After pulses
APD	Avalanche photodiodes
APO	After peak oscillations
BDF	Beam Dump Facility
DC	Dark count
LS	Liquid scintillator
MCX	Micro-coaxial cable
MPV	Most probable value
PCB	Printed circuit board
PCS	Pulse charge spectrum
PDE	Photon detection efficiency
PE	Photo-electrons
PMMA	Polymethyl methacrylate
RMS	Root mean square
SBT	Surrounding Background Tagger
SHiP	Search for Hidden Particles
SiPM	Silicon photomultiplier
SBT	Scattering and Neutrino Detector
SPAD	Single-photon avalanche diode
SPS	Super Proton Synchrotron
WLS	Wavelength-shifting
WOM	Wavelength-shifting Optical Module

1 Introduction

In the 1970s, the Standard Model of particle physics was finalized in its current form when the existence of quarks was experimentally proven. It has since had great success in predicting elementary particles like the top quark or the Higgs boson. Various properties, like the g -factor of the electron, could be calculated with great precision. Time after time, a very good agreement between theory and experiments was found. However, there are several challenges for the Standard Model. For instance, gravity is completely omitted and the Standard Model can not explain the imbalance between matter and anti-matter. A complete description of the universe, a 'Theory of everything', would need to take both gravity and the Standard Model into account. To make progress on the way towards a 'Theory of everything', one therefore has to look for Physics beyond the Standard Model. One way of doing so is to look for undiscovered particles or new interactions that are not predicted by the Standard Model.

Undiscovered particles can be particles that interact very weakly or are only created at very high energies. On that basis, there are three different ways to find particles or interactions beyond the Standard Model: one can use a very high number of interactions, a very high energy of interactions or one uses cosmic particles. Each one of these three defines a frontier. The energy frontier looks for heavy particles at very high energies that are achieved via particle accelerators. The intensity frontier focuses on particles that only interact very seldomly and therefore needs experiments with a very high number of events. The cosmic frontier is looking for particles that are created in space, e. g. in stars or supernovae and have not been detected yet, e. g. dark matter.

This thesis is motivated by the Search for Hidden Particles (SHiP) experiment, which is a proposed beam-dump experiment at the CERN SPS that will work at the intensity frontier. Details will be outlined in the next chapter. This work focuses on the Surround Background Tagger (SBT) part of the experiment. The SBT will use liquid scintillator as a way to detect muons and other charged particles. The goal of this thesis is to test two ways to improve

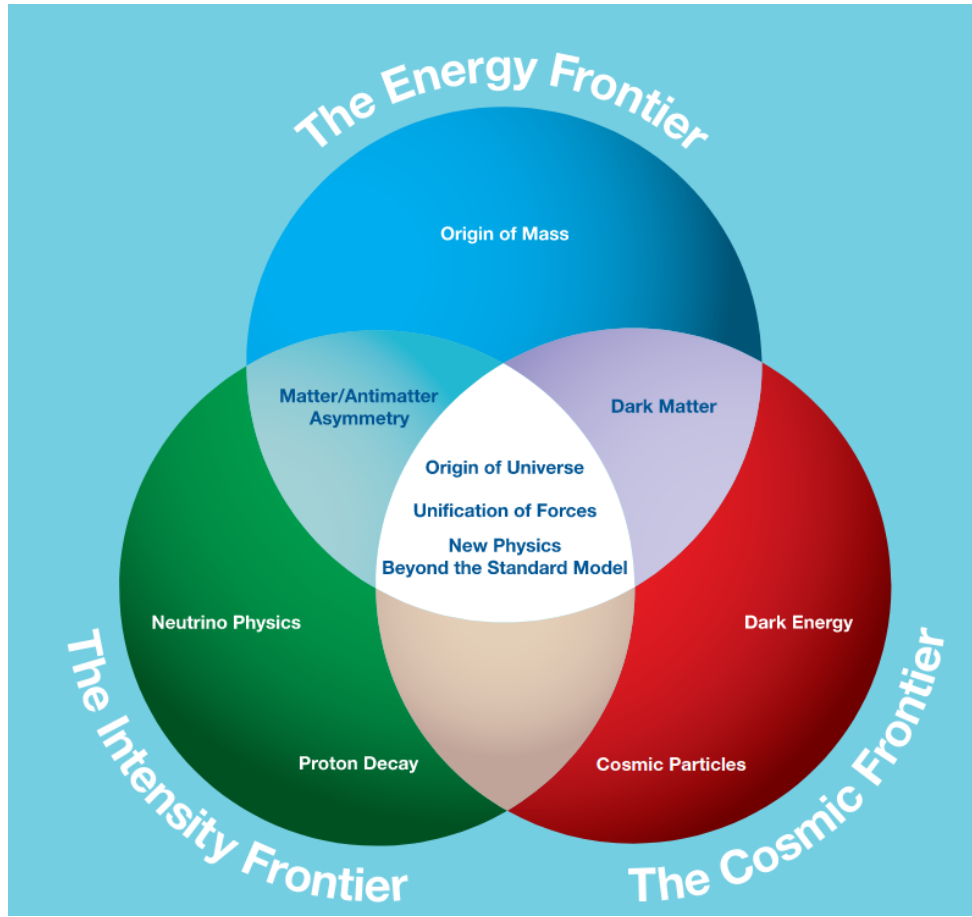


Figure 1.1: The three frontiers of particle physics and related topics, Image credit: [11]

the efficiency of the SBT by testing a procedure to improve the light yield and improving on a previous analysis about the incidence angle of impinging particles. Both will be outlined shortly.

The scintillation light is collected by wavelength-shifting optical modules (WOMs). WOMs are tubes that guide the light through total reflection inside the walls towards the detector at one end of the tube, in this case a ring of silicon photomultipliers (SiPMs) soldered onto a Printed Circuit Board (PCB). The light in the WOM tube can of course travel towards the PCB as well as away from it. In this thesis, it will be investigated whether it increases the light yield of the WOMs if a reflector ring is glued to the end of the WOM tube where no PCB is located. This would increase the detection efficiency. In order to convert the measured light yields to photon numbers, the gain value of three PCBs is measured. The gain indicates the amount of charge that one photon eventually causes in one SiPM.

Additionally, an improvement of the analysis done in [10] is shown. Said study investigated to which level it is possible to recreate the incidence position based only on the PCB response. This might help in the SBT to avoid false vetos and track the muons that enter the decay volume.

2 SHiP Experiment

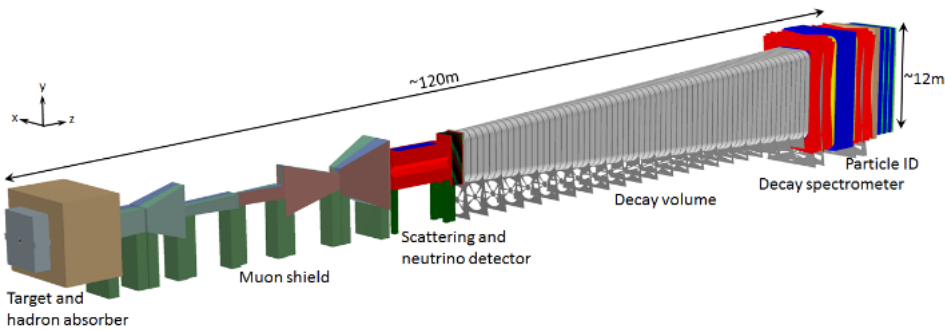


Figure 2.1: Proposed design of the SHiP detector, Image credit:
[30]

The Search for Hidden Particles experiment (SHiP) is a proposed experiment in a beam dump facility at the Super Proton Synchrotron (SPS) situated at CERN on the Prevessin site. Its aim is to look for long lived particles that interact so weakly with known matter that they have not been discovered yet, so-called hidden sector (HS) particles. These could be for example heavy neutral leptons, dark photons, sgoldstinos and axion-like particles. The experiment will work at the intensity frontier, which means that it requires a high number of interactions. SHiP is designed to be a zero-background experiment. To veto events where external particles enter the decay volume, the decay volume is located inside the Surrounding Background Tagger (SBT).

Spills of 4×10^{13} protons with energies up to 400 GeV will be dumped on the beam dump facility (BDF), which will allow SHiP to look at particle masses between 0.1 and 10 GeV. It is planned to get 2×10^{20} proton-target interactions over the course of five years of operation [30, p. 7].

In the following, the planned experiment layout will be described, following fig. 2.1. The protons enter the setup (from the left side in fig. 2.1) and interact with a molybdenum-tungsten (Mo-W) target. The dominant processes at this energy are direct QCD processes, decays of heavy mesons and proton bremsstrahlung.

The interaction of the protons in the target produce large numbers of hadrons, muons and neutrinos that contribute to the background of the experiment. The hadrons are filtered out by the hadron absorber that is located directly behind the target. The hadron absorber is followed by the 35 m long muon shield, which uses a magnetic field of up to 1.7 T [30, p. 17]. The muon shield reduces the flux of beam-induced muons by six orders of magnitude.

The detection components are divided into the Scattering and Neutrino Detector (SND) and the Hidden Sector (HS) spectrometer. The SND consists of an emulsion spectrometer that is located inside a 1.2 T magnetic field and a muon identification system. Its aim is to detect and distinguish neutrinos and anti-neutrinos and look for Light Dark Matter (LDM). The electronic trackers allow a direct measurement of the neutrinos. The LDM is detected through scattering with the absorber material.

Further downstream, the decay volume is located. It has the form of a pyramidal frustum with a length of 50 m. The decay volume is needed because HS particles probably have long decay times in air compared to standard matter. To minimize the neutrino interaction background, the decay volume is evacuated, with a pressure of $\mathcal{O}(10^{-3})$ bar. Then, nearly all of the neutrino interactions take place in the walls of the decay volume, which makes it easier to reject them.

As SHiP is intended to be a zero background experiment, there has to be a possibility to detect non-beam-related particles entering the decay volume. This is done by the Surrounding Background Tagger (SBT), which forms the context of this work. The task of SBT is to detect muons entering the decay volume and tag deep inelastic scattering from neutrinos and muons in the vessel wall. It is planned as a liquid scintillator detector consisting of multiple single cells. The size of one cell will be roughly 50 – 150 cm × 80 cm × 30 cm. Each cell is filled with liquid scintillator and equipped with several wavelength-shifting optical modules (WOMs). The WOMs are viewed on one side by silicon photo-multipliers (SiPMs).

The estimated number of background events during the collection of 2×10^{20} proton-target interactions over five years is <0.1 for beam-induced background events [30, p. 11], $\mathcal{O}(10^7)$ for neutrino and $\mathcal{O}(10^8)$ for muon events

of deep inelastic scattering in the decay volume [30, p. 53].

Behind the decay volume sits the HS spectrometer. Its sensitive area has a width of 5 m and a height of 10 m. It allows for a reconstruction of the decay vertex of HS particles and its identification, using a straw tracker, a set of calorimeters and muon detectors. The muon detector system consists of four stations that are individually divided by muon filters. Low-energy muons are filtered out so that only muons with a momentum of $> 5.3 \text{ GeV}/c$ reach the last station. The reconstruction of the decay vertex helps with the distinction of HS theories.

The final part in the particle identification process is a timing detector with a resolution of $\mathcal{O}(100\text{ps})$ that allows to reject combinatorial background by measuring the time coincidence.

3 Scintillation-based detection mechanisms

3.1 Scintillators

In the context of this work, two different kinds of scintillators are employed: *liquid scintillators* and *plastic scintillators*. Both share the basic principle of emitting light when an ionizing particle crosses the scintillation medium [6]. The scintillation light is produced due to the relaxation of excited states to ground states in the scintillation medium. Scintillators can come as crystals, gases, plastic scintillators or glasses [6]. Chemically, scintillators can be divided into inorganic and organic scintillators. Organic scintillators always contain at least one carbon atom; more specifically, they are aromatic hydrocarbon compounds. As inorganic scintillators usually have longer decay times than organic scintillators ($\mathcal{O}(10 \text{ ns})$ to ($\mathcal{O}(500 \text{ ns})$, [19, p. 9]) and are quite expensive, they are not fit for the use in the Surrounding Background Tagger (SBT), where a high time resolution at low cost is of big interest. The higher the decay time is, the slower the scintillator reacts to an impinging particle, so that the response is smeared out and the time resolution gets worse.

The scintillation mechanism of organic scintillators needs a free valence electron of a molecule in the fluorescent material, that can get excited from the ground state S_0 . “Free” means in this context that the electron does not belong to a specific atom in the molecule; one then says that this electron is in a molecular π -orbital.

The excited states are distinguished into singlet states and triplet states. Singlet states, denoted by the letter S , have a net angular momentum of zero, so that the quantum number of the spin (s) is $s = 0$. In other words, all electrons are paired. In triplet states, written with a letter T , two electrons

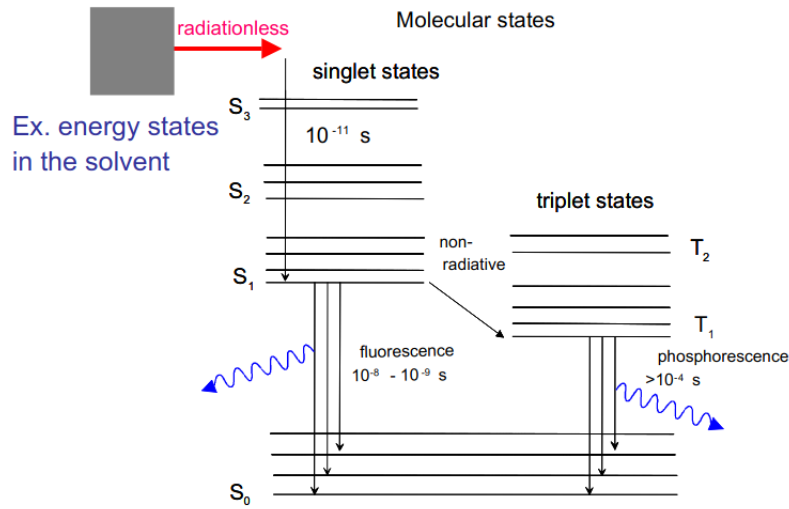


Figure 3.1: Visualisation of the energy levels of a scintillator molecule. The excited singlet (S) and triplet (T) states are separated for a better understanding. Radiationless relaxation is shown between the excited states. Fluorescence and phosphorescence are shown as blue arrows in the corresponding transitions. Figure taken from [6].

are unpaired, resulting in $s = 1$. The energy difference between the excitation levels is in the order of eV. Furthermore, each level is split up into a fine structure which corresponds to the vibrational modes of the molecule. The energy difference between these vibrational levels is in the order of 0.1 eV. A visualisation of the energy states of a molecule is given in fig. 3.1. The ionizing radiation excites the molecule into some state S_1, S_2, \dots or T_1, T_2, \dots , where T_1 is the lowest energy triplet state.

In case the excited state is a singlet state, non-radiative relaxation into the first excited state S_1 takes place after times in the order of less than 0.01 ns. This process is called *internal degradation*. The S_1 then decays to the S_0 state by emitting a photon, with decay times between < 1 up to $\mathcal{O}(10)$ ns after the excitation. This effect is called *fluorescence*.

If the molecule got excited to a triplet state, the same processes as in the singlet case lead to the decay of the excited state to the lowest energy triplet state T_1 . The transition $T_1 \rightarrow S_0$ has a much larger decay time (in the order of μs), as it is forbidden by the multipole selection rules and is called *phosphorescence*. Another relaxation channel is the interaction of two molecules in the T_1 state, leading to $T_1 + T_1 \rightarrow S_1 + S_0 + \text{photons}$. As this requires

the interaction of two molecules, it is also delayed with regard to the incoming radiation. The response of a scintillator to an incoming particle is thus divided into a prompt (fluorescence) and a delayed component (phosphorescence and $T_1 - T_1$ interaction).

Usually, the transition to S_0 ends in one of the vibrational modes of S_0 instead of the lowest possible energy level. Therefore, the emitted photon has not enough energy to excite another molecule from S_0 , which makes the scintillator transparent for the scintillation photons.

3.1.1 Liquid scintillators

The use of liquid scintillator (LS) for the SBT has the advantages of providing a good detection efficiency and sensitivity as well as short response times (typically in the order of a few ns) while still being relatively cheap compared to e. g. plastic scintillators [30]. Additionally, no stress or material abrasion can occur, contrary to plastic scintillators. LS have successfully been used in many other experiments as e. g. bis-MSB and PPO at JUNO [7] and water-based liquid scintillator at THEIA [2], so their characteristics are well known and their reasonable usage has been demonstrated many times.

Usually, LS consist of a fluorescent material and a solvent; pretty often, a third material is added as a wavelength shifter. The reason to use solvent is to create a liquid where the fluorescent material is dissipated evenly on the one hand (e. g. if the fluorescent is a powder as it is the case for PPO) and to absorb and to guide the energy of the incoming radiation to the fluorescent material on the other hand. This energy transport can happen through different channels: non-radiative dipole-dipole interactions, the so-called *Foerster transfer*, radiation and impact of excited solvent molecules on scintillator molecules.

In the context of the SHiP experiment, the fluorescent material is 2,5-diphenyl-oxazole (PPO) and the solvent is linear alkylbenzene (LAB). LAB was chosen over the other candidates phenyl-o-xylylethane (PXE) due to its higher light yield (order of 10%) and pcedocumene (PC) due to safety concerns concerning the high flammability of PC [29]. Although another scintillator, 1-phenyl-3-mesityl-2-pyrazoline (PMP), shows lower self-absorption¹, studies

¹re-absorption of scintillation photons by the scintillator

have shown that the response time² is much bigger than for PPO [29]. The emission spectrum of PPO peaks at a wavelength of 385 nm [4].

More specific details about the LS are still being tuned. For instance, tests are being made on adding paraffin oil to the scintillator-solvent mixture in order to increase its transparency or on adding vitamin E to protect the LS when being exposed to oxygen [30].

3.1.2 Plastic scintillators

Quite similar to LS, plastic scintillators consist of an organic scintillator (here called fluor) which is in this case not solved in a liquid solvent, but rather in a solid polymer matrix (called base). This is either accomplished by the dissolution of the fluor before the bulk polymerization or by associating it later to the polymer. Usually, the concentration of the fluor in the solvent is in the order of 10 g/l.

Plastic scintillators also offer fast response times, in the order of a few ns, but are usually more expensive than liquid scintillators. They withstand water, lower alcohols and fats, but are sensitive to organic solvents. In praxis, one has to handle them wearing gloves in order to avoid sweat damaging the material. For this work, plastic scintillators with a Polyvinyltoluene base are being used (cf. sec. 4.2).

3.2 Wavelength-shifting optical modules

In previous studies involving scintillation light, the light was often detected using photo-multiplier tubes (PMTs). However, the use of wavelength-shifting optical modules (WOMs) for light detection has the advantage of being cheaper, easier to install and having a lower noise level than PMTs. The proposal of using WOMs in combination with liquid scintillator was made for IceCube Gen 2 and is based on [26]. The WOM design was adapted for the use in the SHiP SBT (cf. sec. 2).

A WOM is a tube made of a UV-transparent material that collects photons and guides them towards a read-out. The photons travel through the WOM walls due to total reflection (cf. fig. 3.2). The WOMs used for this work are

²The time in which the LS responds to an incoming particle

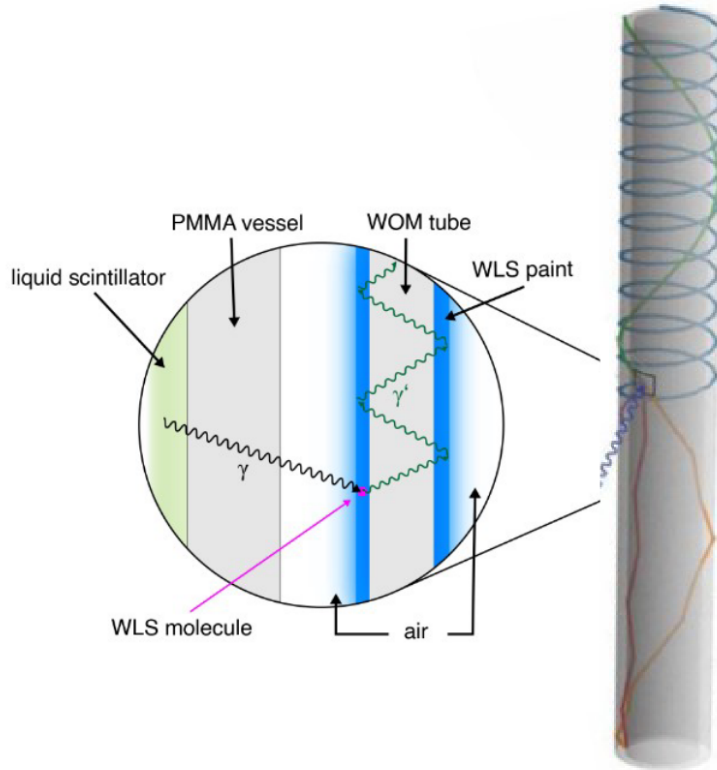


Figure 3.2: Sketch of a WOM tube and possible light paths inside a WOM tube (shown on the right). The magnification shows principle of the WOM including the WLS paint: The scintillation light is created in the LS. It crosses a PMMA vessel and the air gap, which ensures total reflection on the walls of the WOM once the light travels inside the WOM tube. In the WLS paint (blue area), the wavelength of the light is shifted and the photons are re-emitted into the WOM tube (green arrows).

Figure taken from [17] and based on [25].

made of polymethylmethacrylate (PMMA), as is planned for the SHiP SBT. They are 230 mm long and have an outer diameter of 60 mm. The wall thickness for this study is 3 mm.

PMMA has a refractive index of $n_{\text{PMMA}} \approx 1.5$ [18]. With air on both sides of the WOM wall, this means that the photon will be totally reflected if it hits the wall with an incidence angle smaller than

$$\theta_c = \arcsin \left(\frac{n_{\text{air}}}{n_{\text{PMMA}}} \right) \approx 41.8^\circ \quad (3.1)$$

The air gap between the LS and the WOM wall is ensured by embedding the WOM inside of a dedicated PMMA vessel, shown in fig. 3.3. Neglecting possible transport losses inside the PMMA, the fraction of photons with $\theta \leq$



Figure 3.3: Picture of a (defect) PMMA vessel. The WOM is inserted to ensure an air gap between the liquid scintillator and the WOM tube.

θ_c is roughly 73% [26]. This is thus the theoretical maximum of the capture efficiency.

At one end of the WOM tube, the photons are detected by a ring of silicon photo-multipliers (SiPMs, cf. sec. 3.3). For this work, the wavelength of the emission peak of the LS in use (cf. fig. 3.4a) is at 360 nm and 385 nm (ultra-violet) [9]. The highest photon detection efficiency (PDE) of the used SiPMs (cf. fig. 3.5), however, lies at wavelengths of approximately 450 nm (blue). To guarantee an efficient photon detection, a wavelength-shifting (WLS) paint that shifts the wavelength of the scintillation light towards the region of the highest PDE of the SiPMs (cf. fig. 3.4b) is applied to the WOM wall. The coating is done by mechanical dip-coating, which means that the WOM is dipped into the WLS paint and removed after a short time.

The used paint is a mixture of the wavelength-shifters Bis-MSB and p-Terphenyl, the solvent Toluene and the binder Paraloid B72 [8]. For 100 ml Toluene, 25 g Paraloid, 0.15 g Bis-MBS and 0.3 g p-Terphenyl were used.

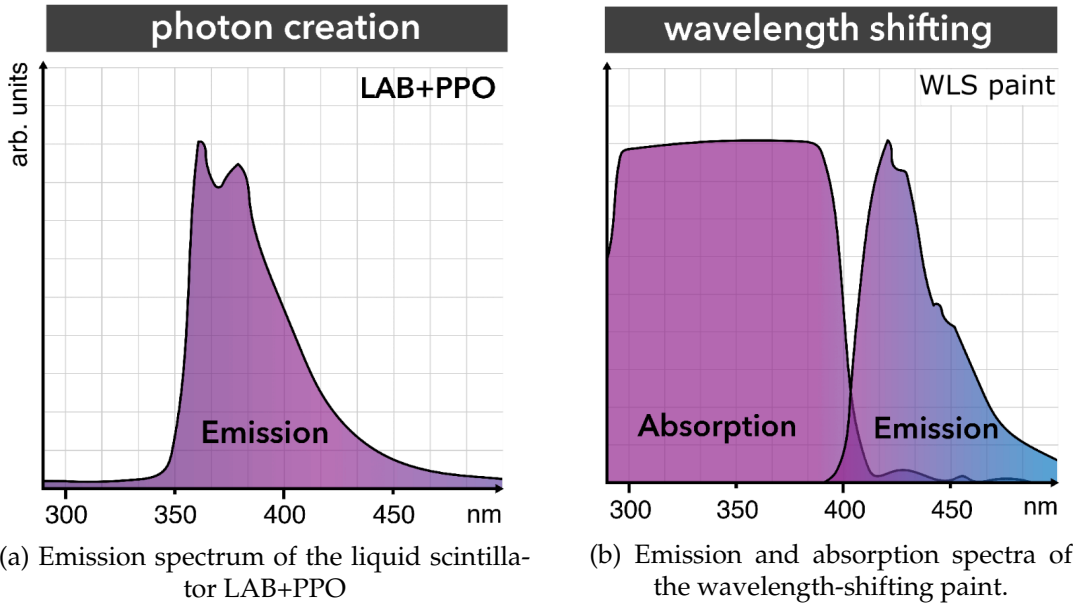


Figure 3.4: Emission spectrum of the LS and emission and absorption spectra of the WLS. The peak wavelength of the LS emission lies well within the absorption range of the WLS paint. The emission peak wavelength of the WLS paint is close to the peak of the photon detection efficiency of the SiPMs given in fig. 3.5. The units on the y axis are arbitrary. Figure from [32] and based on [8]

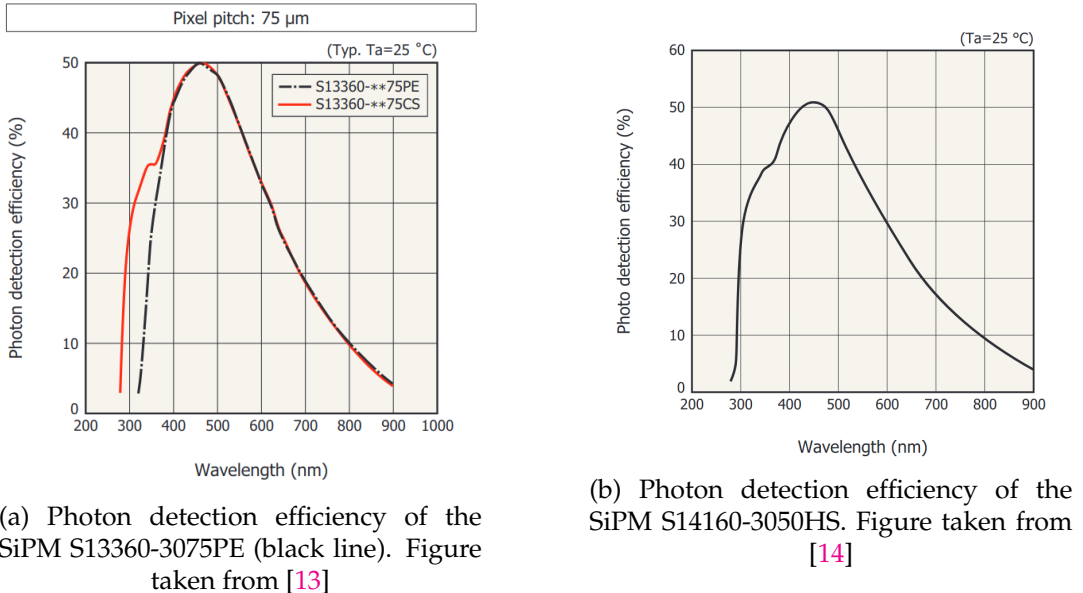


Figure 3.5: Photon detection efficiency of the used SiPMs without crosstalk and afterpulses. The PDE was measured at 25°C. In both cases, the efficiency peaks at a wavelength of approximately 450 nm.

The principle of the WLS paint is based on fluorescence, like scintillators. The emitted photon has a longer wavelength than the absorbed one, because a certain amount of energy was emitted in a non-radiative fashion (cf. sec. 3.1), a phenomenon called *Stokes shift*. The secondary photons are emitted isotropically by the WLS paint.

Detected photons generally did not take a straight path to the SiPM array inside the WOM tube, but rather travelled e. g. in a spiral (cf. fig. 3.2). Therefore, they do not necessarily reach the SiPM array on the same side where they were created and it is not clear whether any information about their origin - and with that about the incidence position of the charged particle in the LS - can be obtained. Further details will be discussed in sec. 7.3.

On the side of the WOM tube that is not equipped with a readout system, some of the photons are also reflected. One goal of this work is to check whether these photons contribute substantially to the light yield of the WOM tube. For this purpose, black foil was glued to the tube to suppress total reflection. Further details and results on this are presented in sec. 6.5.

Furthermore, it was studied whether the light yield can be increased if the reflection at the end of the WOM is supported by a mirror. Reflective mylar foil was glued to the end of the WOM with an optical glue and the light yield with and without reflector was compared. The results are discussed in sec. 6.4.

3.3 Silicon photo-multipliers

The Silicon photo-multipliers (SiPMs) form the other part of the light detectors that are used in the LS. While the WOM tube collects the light, the SiPMs detect it with an output voltage signal that can then easily be read out. Their usage has many advantages, such as lower prices than PMTs, a high efficiency, good time resolution, immunity to magnetic fields and a low operation voltage.

SiPMs are made of doped silicon, which is semiconducting. Semiconductors are best understood in the band theory, where the energy states that electrons can occupy are generalized from the single-atom discrete levels to quasi-continuous *bands*.

In a semiconductor and also in insulators, there is an energy gap, the *band gap*, between the *valence band* and the *conduction band*. The valence band is the first band with an energy lower than the *Fermi level*³, while the conduction band is the first band with an energy higher than the Fermi level. In order for a material to be conductive, there have to be delocalised electrons in a partially filled band. The charge carriers are the negatively charged electrons e or positively charged holes h .

The band gap for semiconductors is smaller than for insulators, so that semiconductors are neither good insulators nor good conductors at room temperature (as enough electrons can be excited to the conduction band); hence the name.

The conductivity of semiconductors can be varied and controlled by a process called *doping*. Doping is the insertion of impurities into the semiconductors. Speaking in the band model, doping decreases the energy difference between the valence band or the conduction band and the Fermi level, so that the probability of them being partially filled is much bigger. As Silicon photomultipliers will be used in this work, doping of silicon will be further explained.

Silicon has four valence electrons. Doping is now done by adding atoms that have either five or three valence electrons to create a surplus of electrons or holes, respectively. The layer of the material where impurities with five valence electrons have been inserted is called *n*-layer, whereas a section that was doped with impurities with three valence electrons is called *p*-layer.

When *n*- and *p*-layers are combined, a transition region develops, called the *pn*-junction. In this area, electrons and holes recombine, so their charge cancels each other out and a region without free charge carriers is established. If a photon crosses the *pn*-junction, it can transfer its energy to an electron and create an electron-hole (*eh*) pair.

The probability of a photon interacting in the *pn*-junction scales with size of the *pn*-junction. To increase the sensitive area, it is common to add another neutral layer (*i*) into the *pn*-junction. Although photodiodes that employ this

³The amount of work it would take to add one electron to the system

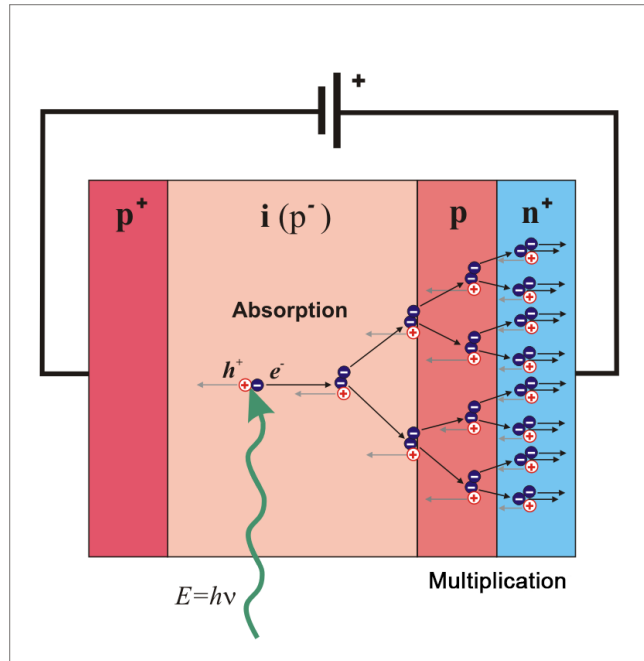


Figure 3.6: Principle of an APD. Photons are absorbed in the i -layer, where they create eh -pairs. They are accelerated towards the edges of the photo-diode. In the p -layer, the photo-electrons can create new eh -pairs through impact ionisation, so that the current is multiplied. This is called the avalanche. Figure taken from [20].

technique, so called *pin*-photodiodes, have increased sensitivity compared to *pn*-photodiodes, they are usually not sensitive enough to detect single photons. To increase the detection sensitivity, *avalanche photodiodes (APDs)* have been developed.

APDs feature an additional multiplication zone, which increases the photo-voltage. It is realised by inserting another p -layer between the i - and the n -layer. The principle is shown in fig. 3.6: When a photon impinges on the i -layer, it creates an eh -pair. A reverse bias voltage U_{bias} is applied to the diode. The electron now moves towards the anode (and the hole towards the cathode), whereby the electron is accelerated. While crossing the p -layer, it can create new eh -pairs by impact ionisation. These again are separated and accelerated and can create eh -pairs themselves. This causes an avalanche of electrons to be detected in the end, leading to currents much higher than in *pin*-photodiodes. For the avalanche to take effect, a certain voltage has to be applied. This is called the avalanche breakdown voltage $U_{\text{breakdown}}$. The APD response is linear to the number of incoming photons.

When an APD is operated with a voltage that is high enough that one eh -pair can create a self-sustaining avalanche current, it is said to be in *Geiger mode*. The reverse bias voltage is then higher than the breakdown voltage. The difference between bias voltage and breakdown voltage is defined as the overvoltage U_{over} .

$$U_{\text{over}} = U_{\text{bias}} - U_{\text{breakdown}} \quad (3.2)$$

As this allows the detection of single photons, the system is also called *single-photon avalanche diode (SPAD)*. The impact of a photon can be measured with a time jitter in the order of picoseconds [5].

The avalanche created by the impact of a single photon could in theory be infinitely amplified by a SPAD in Geiger mode, so that a mechanism to stop the avalanche has to be implemented. This is done by active and passive quenching resistors, which are connected in series with the diode and lower the bias voltage so that $U_{\text{bias}} < U_{\text{breakdown}}$, so that the avalanche ends. After the quenching, the bias voltage has to be turned up again to allow photon detection. This means that there is a dead time of typically $\mathcal{O}(10 - 50)$ ns after the detection of a photon in a SPAD.

SiPMs are modules consisting of several SPADs. Each SPAD together with a quenching resistor forms a pixel. The pixels are connected in parallel, as shown in fig. 3.7, which means that the output current is proportional to the number of triggered pixels. The number of pixels per SiPM is in the order of 1000; in the context of this work 1600 and 3531, cf. table 4.1. Choosing the right amount of pixels is important for the application of SiPMs: it should be big compared to the number of incident photons. This allows to assume that each pixel is hit by only one photon at a time. Then, the amount of triggered pixels is equal to the amount of detected photons. If the number of photons was higher than the number of pixels, several photons would impinge on one pixel and one could not infer the number of detected photons anymore.

Besides the number of pixels, the pixel pitch is an important quantity for the characterisation of SiPMs. The pixel pitch is the distance between the centre of a pixel to the centre of the pixel next to it. SiPMs usually have pixel pitches of 10 μm to 100 μm .

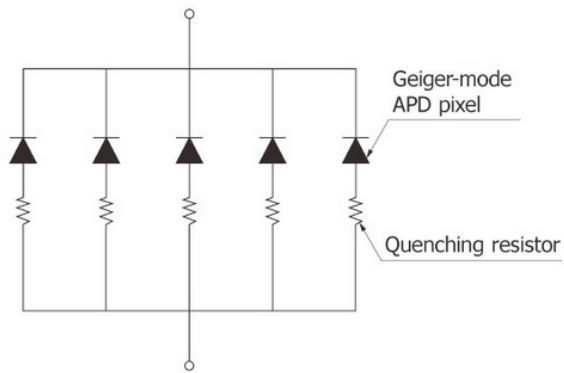


Figure 3.7: Structure of a SiPM. Several single cells consisting of a SPAD and a quenching resistor in series (called pixels) are connected in parallel. Figure taken from [15]

4 Cosmics setup and SiPM calibration setup

4.1 Readout hardware

4.1.1 SiPMs and PCBs

Two different kinds of silicon photomultipliers (SiPMs) were used over the course of this work: S13360-3075PE and S14160-3050H. Both SiPM series are produced by Hamamatsu. The SiPMs must fit to the 3 mm wall of the WOM tube, they should have a low dark count rate and a high photon detection efficiency. In table 4.1, important parameters of them are listed for comparison. The SiPMs are arranged in a ring and soldered onto a printed circuit board (PCB). As the PCB should cover the entire top of the WOM tube, its diameter was chosen to be 60 mm. Three different PCBs were used in this work: PCB C and PCB D were designed and manufactured at the University of Geneva, PCB J was designed and manufactured at the Forschungszentrum Jülich. As indicated in table 4.1, PCB C and D used SiPMs of the series S13360-3075PE, whereas PCB J used S14160-3050HS SiPMs.

On the PCBs, the 40 SiPMs are organized in groups of five SiPMs, to match the readout with the eMUSIC-Board (see sec. 4.1.2). Each group forms one *channel*. Each individual SiPM can be switched on and off by using a dedicated dip switch at the back side of the PCB. The channels are read out by a SAMTEC LSHM readout adapter.

4.1.2 eMUSIC-Board

The electronic signals by the SiPMs are collected by the eMUSIC Miniboard v2 by Scientifica [27]. It supports an eight channel readout via an application-specific integrated circuit (ASIC). The eMUSIC board can pre-amplify and sum input signals and apply filters such as pole-zero cancellation. The eMUSIC board is powered by two low-voltage (LV) lines of 6.5 V each. It also

Name	S13360-3075PE	S14160-3050HS
used for PCB	C&D	Jülich (J)
Effective photosensitive area (mm²)	3.0×3.0	3.0×3.0
Pixels/SiPM	1600	3531
Pixel pitch (μm)	75	50
Breakdown voltage (V)	53 ± 5	38
typical dark current (μA)		0.6
maximal dark current (μA)		1.8
typical dark count rate (kc/s)	500	
maximal dark count rate (kc/s)	1500	
Maximum photon detection efficiency (PDE) (%)	50	50
Crosstalk probability (%)	7	7

Table 4.1: Characteristic values of SiPMs. Values taken from [13] and [14] provided by Hamamatsu. The dark count (DC) threshold is $0.5N_{pe}$. The measurement conditions were $T = 25^\circ\text{C}$, $U_{\text{over}} = 3.0$ V for S13360-3075PE, $U_{\text{over}} = 2.7$ V for S14160-3050HS

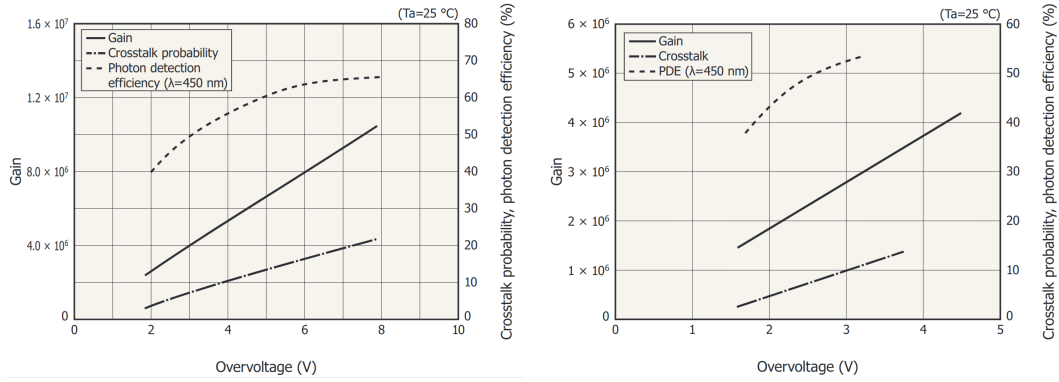


Figure 4.1: Gain (solid line), crosstalk probability (dashed and dotted line) and photon detection efficiency at 25°C for the two kinds of SiPMs that were used.

powers the SiPMs with a high-voltage (HV). Both LV and HV are lead to the board via one connector. As explained in [27], there is an offset in the HV of $U_{\text{offset}} = 891 \text{ mV}$, so that the actual bias voltage U_{bias} that is applied to the SiPMs is related to the power that is set on the power supply U_{set} by

$$U_{\text{bias}} = U_{\text{set}} - U_{\text{offset}}$$

Different HV were applied, the specific values of U_{set} will be given in the respective section. As the input of the WaveCatcher (cf. chapter 4.1.3) is micro-coaxial cable (MCX), but the output of the eMUSIC board is Pin, an adapter board from Pin to MCX by Scientifica is installed in the setups. The eMUSIC board is clipped directly onto the adapter board.

Changing the settings of the eMUSIC board

Several parameters of the eMUSIC board can be changed via a USB connection to a computer. A LED shows USB connection, so it is important to always unplug the USB cable before taking a measurement in order to avoid the LED light. When the eMUSIC board is connected to a computer, the eMUSIC software `mini_music.exe` has to be run through the console of the connected computer. Several commands can be found in [27].

For the following measurements, disabling the pole-zero cancellation is of great importance. In order to do this, the command `mini_music.exe config -t -a -e 0 1 2 3 4 5 6 7 -P COM4` has to be executed. This enables trans-impedance mode, attenuates the pole-zero cancellation, enables channels 0 to 7 and passes this configuration to USB port COM4. After this command, `mini_music.exe vdc_calib -P COM4` should be executed to allow the correct calibration of the eMUSIC board.

4.1.3 WaveCatcher

The digitization of the electronic signal takes place in WaveCatcher by Caen [22], which is equipped with a SAMLONG analogue memory. There are 16 possible input channels. When using the SiPM calibration setup, channels 0 to 7 were assigned to the SiPM channels and channel 8 is used as the trigger channel, by connecting it to the trigger output of the laser. When the SBT prototype is used, channels 0 to 7 are again the SiPM channels and channels 10 to 13 are connected to the PMTs viewing the plastic scintillators (cf. sec.

4.2). In each channel, 1024 samples can be processed. With a sampling rate of $0.4 \cdot 10^9$ samples/s to $3.2 \cdot 10^9$ samples/s, this results in a length of 2560 ns to 320 ns of a recording; this will be referred to as “time window” as of now. The time window used for all measurements was 320 ns, so the highest sampling rate was used. The data taken in all channels during the time window will be called an *event*; all events form one *run*.

The readout of the digitized data is realized via a USB interface. A user interface on a computer (available at [22]) allows a real time monitoring of the measurements. When measurements are taken, usually a fixed number of events is defined beforehand and the measurement stops automatically. For troubleshooting, there is also the continuous mode where the data is not stored and the measurement continues indefinitely. For first measurements, version 2.9.16 of the WaveCatcher software was used. However, a bug occurred, which caused the pedestal correction to be deactivated whenever the trigger delay value was changed. This led to the recorded voltage only taking values that are multiples of the LSB value of the ADC, 600 μ V. In version 2.10.1, this bug was fixed, so only measurements with this software version will be taken into account in this work. The software also gives the possibility to adjust several settings, such as the trigger conditions.

For the laser setup, the trigger of the laser was used. This means that the recording of one event was started as soon as the falling edge of the signal in channel 8 sinks below -0.31 V. For the cosmics setup, a coincidence trigger was set for the falling edge of the channels 10 to 13 of the PMTs. It is important to keep in mind that the trigger signal as well as the PMT signals have only negative voltages, so that the falling edge is the beginning of the signal.

The recorded data is stored in .bin files where each one contains 500 or 1000 events. The size of one event varies between roughly 18 and 40 kB. This makes the storage requirements quite high, since e. g. each run of one measurement with the cosmics setup (8000 events) takes up 248 MB. Two different algorithms were used to process the data and reduce the used memory. Both will be described in chapter 5.

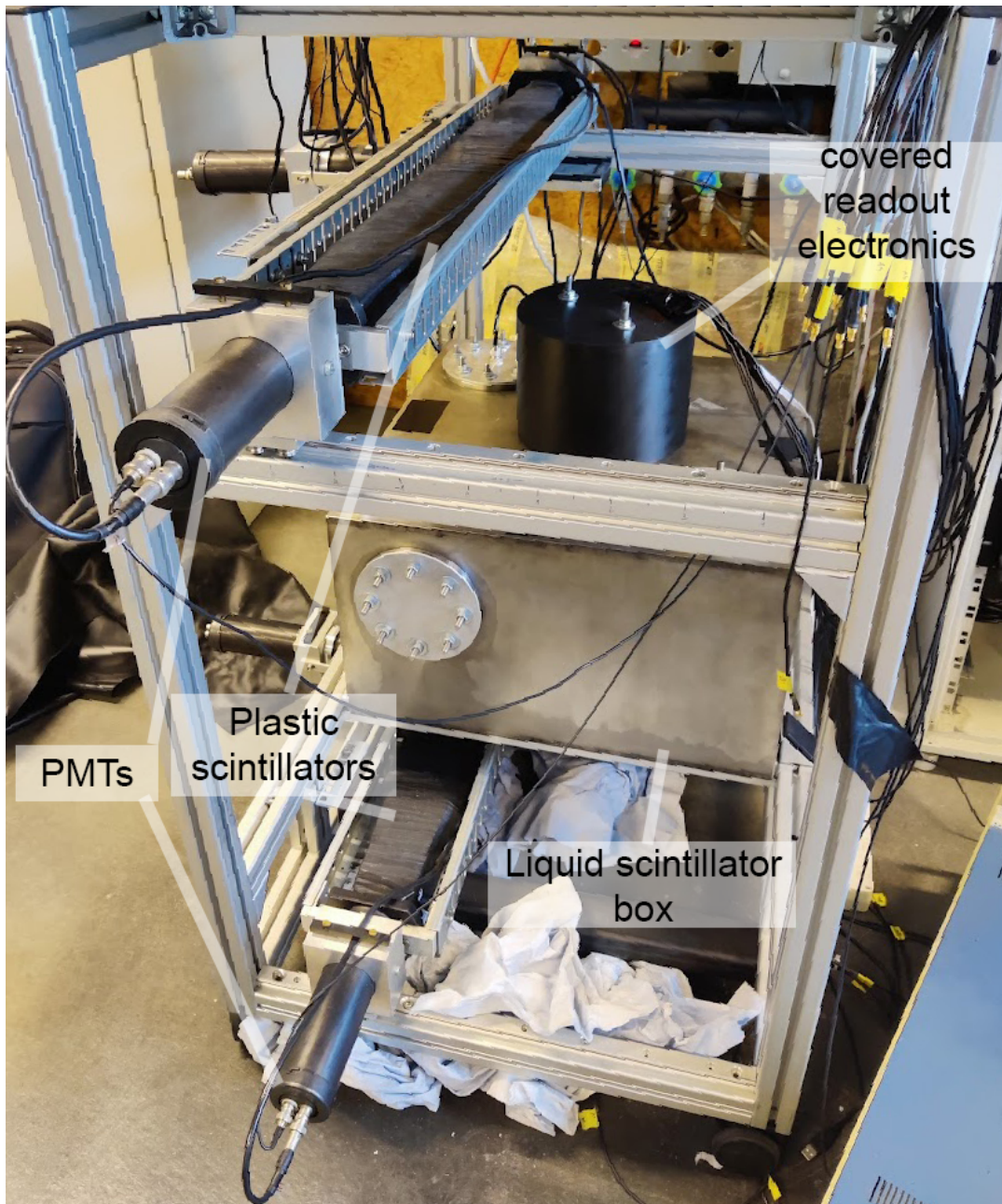


Figure 4.2: Photo of the cosmics setup with the parts labelled.
The readout electronics are shown in detail in fig. 4.4.

4.2 Cosmics setup

The cosmics setup consists of a liquid scintillator box and a set of plastic scintillators. The liquid scintillator box has outer dimensions of $50.4\text{ cm} \times 50.4\text{ cm} \times 25\text{ cm}$. Several holes allow the insertion of WOM tubes, however, all measurements were made using only one WOM tube, which is centered in the box. The WOM tube is protected against light with a black cylinder that was screwed onto the box and insulating tape. The unused holes are

sealed with metal caps that are secured by bolts, visible in fig. 4.2 as silver circles. Further details on the fixation of the WOM tube are provided later on.

The box is filled with 52.7 l of liquid scintillator (LS) made of LAB and PPO. The concentration of PPO in LAB is 2 g/l. Different LS materials were studied in [32] and PPO was concluded to be preferred due to its small response time to muon events. The argument to use LAB is its cost efficiency and practical reasons such as beneficial safety regulations (cf. sec. 3.1.1).

When the WOM tube is inserted in the setup, it is contained in a polymethyl methacrylate (PMMA) vessel (fig. 3.3). This means that there is a layer of air between the WOM tube and the LS. At the bottom of the WOM tube, there is a PMMA spacer that minimizes the area of direct contact between the PMMA vessel and the WOM tube to 12 mm^2 [32]. The SiPMs used for readout are mounted on a PCB, which is located on the top side of the WOM tube. It is very important to minimize the contact area to the PMMA vessel as well as to stabilize the PCB. Both is achieved by metal sliders that are screwed to the SBT prototype box. A picture of the slider system is shown in fig. 4.3. There are four sliders; each one consists of a bottom piece with dimensions of $1.2 \text{ cm} \times 2.1 \text{ cm} \times 3.0 \text{ cm}$ which fixates the WOM tube and a top piece with dimensions of $1.2 \text{ cm} \times 0.7 \text{ cm} \times 1.9 \text{ cm}$ that is screwed onto the bottom piece and fixates the PCB. The contact between slider and WOM tube or PCB, respectively, is formed by a ePTFE disc with a radius of 2 mm and a thickness of 3 mm which protects the WOM tube and the PCB from damage by the aluminum of the slider.

To install a WOM tube in the PMMA vessel, one first needs to clip the PMMA spacer to the bottom of the WOM tube. In case that the spacer falls off during installation or deinstallation, it has small holes which allow to remove it from the PMMA vessel. After carefully inserting the WOM tube into the PMMA vessel, one needs to adjust the sliders. While the top pieces of the sliders are in an outward position, one first moves the WOM tube so that it has no contact to the WOM vessel, adjusts the bottom parts of the sliders accordingly and tightens the screws. Using the area of the ePTFE discs, a contact area of 50 mm^2 is calculated [32]. No excessive force should be exerted on the tube. The SiPM array should be placed centrally on the WOM tube in a way that the covered area is equal all around the circle. To avoid a layer of air,

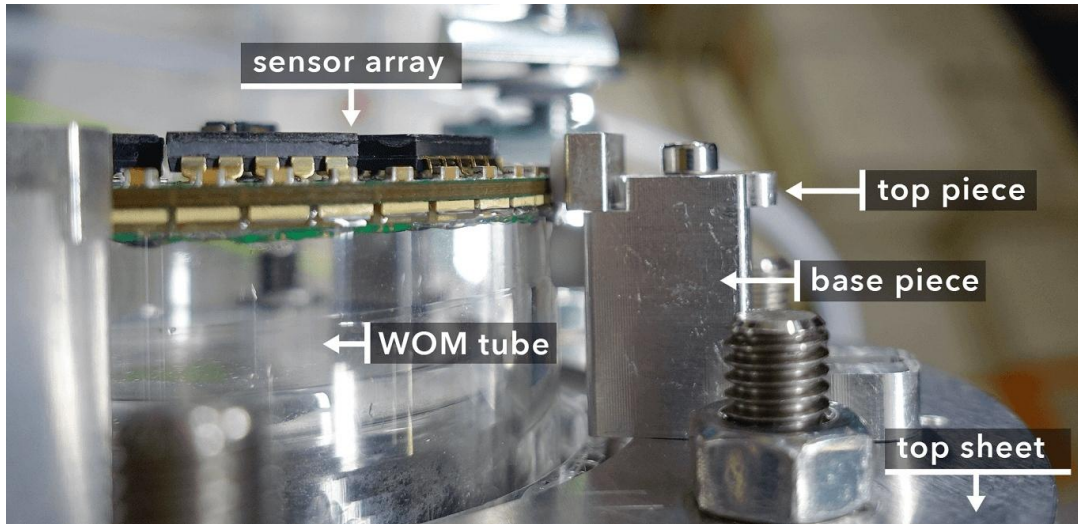


Figure 4.3: Close-up of the holding system of the WOM tube (base piece) and the SiPM array (top piece). Figure taken from [32, p. 36].

which would cause reflection and therefore loss of detection efficiency, optical gel is applied on the SiPM array. Medium-viscose optical gel Baysilone by Bayer-Silicones was used. It was applied directly from the tube onto the SiPMs. Afterwards, the SiPM array was placed as described on the WOM tube and fixated by the top parts of the sliders. Now, the WOM tube and the SiPM array are fixed in the transverse directions.

To fix the SiPM array also in the longitudinal direction and to offer a way to read out the SiPM array, the so-called bridge is used. A picture of the SiPM array on top of the WOM, the bridge and the adapter board (see chapter 4.1.2), can be seen in fig. 4.4. It is a piece of aluminum with the dimensions $6\text{ cm} \times 0.4\text{ cm} \times 13\text{ cm}$ which is screwed to two long rods that stick out of the LS box. Several holes allow the attachment of the read out electronics, which are discussed in sec. 4.3. Washers and nuts are used to fix the bridge in the correct height, so that it does not push down on the SiPM array.

As described before, the PCB and an adapter board are covered by a hollow black cylinder made of polyoxymethylene (POM). It has an inner diameter of 19.8 cm and an outer diameter of 20.5 cm. The height amounts to 15.5 cm and the thickness of the upper wall is 0.7 cm. The cylinder has holes to fix it to the same rods that hold the bridge in place and an elongated hole through which the cables to and from the SiPM array are laid. These holes are sealed by black insulation tape when measurements are taken. Additionally, a black

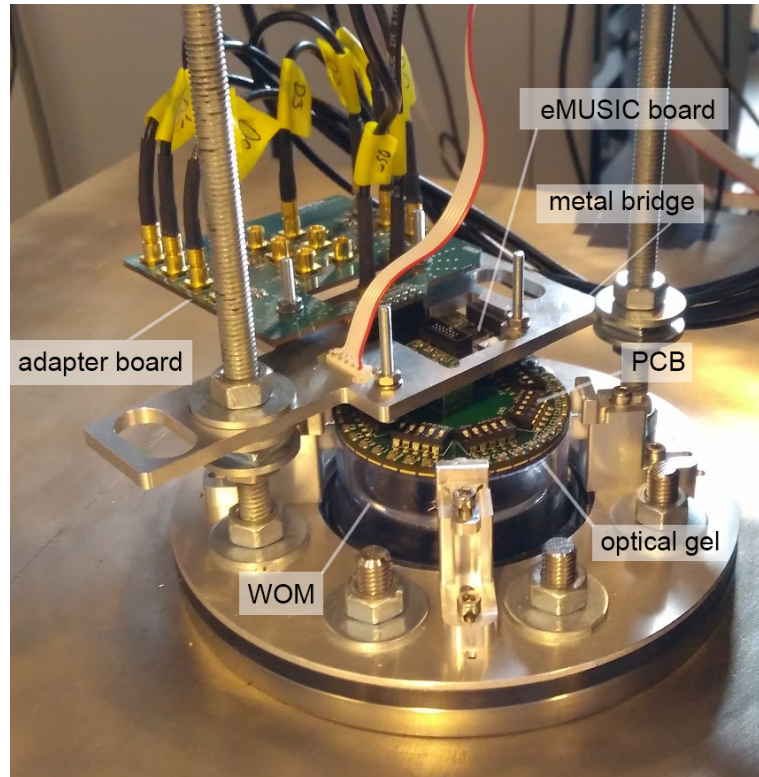


Figure 4.4: Foto of the installed SiPM array on top of the WOM tube in the SBT prototype. As described in chapter 4.2, a metal bridge is used to fixate the SiPM array and allow it to be clipped to the adapter board. The entire system is covered by a black cylinder when the setup is in use.

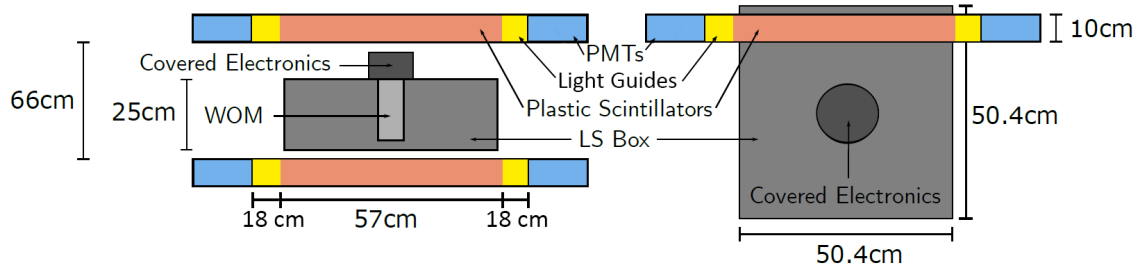


Figure 4.5: Front view (on the left) and top view (on the right) of the SBT prototype. The liquid scintillator box is coloured grey, with the position of the WOM inside the box highlighted in light grey. The plastic scintillators are coloured orange, the light guides at the end yellow and the PMTs blue. Figure based on [10, p. 14].

foil covered the setup.

Two plastic scintillators of the type NE-110 by Eljen Technology are installed (highlighted in fig. 4.2), one above and one below the scintillator box. Both are 57 cm long. At each end of a plastic scintillator, a light guide with a length of 18 cm was attached to collect light and guide it towards the PMTs. To get a better spatial notion, the front and top view of the cosmics setup is shown in fig. 4.5. At each end of the plastic scintillators, there is one photomultiplier tube (PMT) of the type XP2008 by Koninklijke Philips N.V. The plastic scintillators are used as a trigger system to know when a particle passes through the box (cf. sec. 7.1).

4.3 SiPM calibration setup

In order to determine certain characteristical values of the readout SiPMs (cf. section 4.1), a laser setup was used. It consists of a black acrylonitrile-butadiene-styrene (ABS) box with the dimensions 50 cm × 50 cm × 26.5 cm. The components are attached to a breadboard. A 403 nm PiL040XSM laser by A.L.S GmbH is used to create light pulses with a duration of 30 ps and a power of up to 10 mW. It is controlled via a control unit. This control unit offers the possibility of a trigger output which is used to synchronise the start of an event measurement and a laser pulse. The pulse repetition rate is up to 120 MHz. The intensity of the laser is controlled via a so-called “tune value” which does not scale linearly with the power. The light of the laser is guided in a laser fiber and passes an attenuator, an ADAFC1 fiber mating sleeve by

Thorlabs, which reduces the light intensity even further. The attenuator connects two optical fibers, where one can vary the distance that the light has to travel with a rotary wheel. The longer the distance, the smaller the light intensity becomes due to reflection at the fiber output. At the end of the optical fiber, an optical diffusor, the DG10-220 by Thorlabs, ensures the even illumination of the SiPM array. The SiPM array is plugged into an adapter board which itself is connected to the WaveCatcher (cf. section 4.1). The readout and power cables as well as the optical fiber are guided into the box via a hole in the wall that is screwed close when the setup is in use. To protect experimentators, the laser is connected to an interlock that automatically shuts it off when the box is opened.

Two modes of operation of the laser setup can be distinguished: to determine the dark count (DC) rate of the SiPMs, the laser is turned off, so that the trigger signal of the control unit triggers although there is no laser signal. Hence, all events that are recorded in this mode are due to dark counts and noise. When the laser is switched on, one can e.g. determine the calibration value of the SiPMs.

4.4 Dark counts, crosstalk and afterpulses

Apart from the electronic noise created by the readout system, there are three sources of unwanted signals in the SiPMs: dark counts, crosstalk and afterpulses.

Thermal excitation can lead to the measurement of so-called **dark counts (DC)**, which lead to the detection of one or more photons without a scintillation or laser photon hitting the SiPM. DC are caused by thermally generated electron-hole pairs (through defects with energy levels near $E_g/2$).

Additionally, another effect that causes dark counts can be seen when the bias voltage is high: electrons can tunnel from the valence to the conduction band. Both DC causes are more likely for higher temperatures and higher bias voltages, making the DC rate dependent on both of these factors.

When a pixel in a SiPM, so a single SPAD, is triggered, an avalanche is created (cf. sec. 3.3). This avalanche is sustained by electrons being accelerated and creating secondary *eh*-pairs. However, also the creation of secondary

photons is possible. These photons can then be detected in the same pixel or even travel to another pixel and lead to a signal there. This process is called **crosstalk (XT)**. Depending on whether the photon is absorbed in the depleted region or in the non-depleted region, the time of detection varies between prompt and delayed, respectively. Crosstalk can therefore be divided into prompt and delayed crosstalk (P-XT and D-XT respectively). While P-XT leads to a higher peak, indicating naively that one has e. g. detected two photons instead of one at the same time, D-XT leads to two separate peaks. This looks as if two photons have been detected shortly after each other. Both processes also depend on the bias voltage. To minimize crosstalk probability, metal trenches dividing the SiPM pixels can be built in [24].

A third cause for signal distortion can be afterpulses (AP). They are generated by charge carriers in the avalanche that are trapped by impurities in the SiPM. After they are released, they can start a new avalanche themselves. Depending of the duration of their delay, the secondary avalanche can lead to a smaller voltage than the original one - if the SPAD is in the recovery phase after the quenching started - or even to the same amount of voltage. The probability of APs also depends on the bias voltage

It is not possible to distinguish a dark count from an actual detected photon by signal shape or other properties. Moreover, the number of triggered pixels can be altered by crosstalk without a possibility to completely exclude this. All noise effects are dependent on the bias voltage, so that a compromise between a high gain and a high noise has to be made. In general, the signal to noise ratio gets worse the bigger the overvoltage is.

5 Data analysis, calibration and light yield comparison

5.1 Event properties

As described in sec. 4.1.1, the used PCB is equipped with 40 SiPMs organised in groups of five. Each group is read out by one channel on the eMUSIC board and subsequently by one channel in the WaveCatcher. An *event* means all recorded values of voltage over time for a fixed period of time - in this work 320 ns - in one channel. Therefore, more than one SiPM can contribute to an event in a channel. The measured values of one event in one channel are filled into a histogram with 1024 bins to create the so-called *event waveform* or short only *waveform*. An example of an event waveform is given in fig. 5.2. First, event properties of single SPADs will be discussed. Then, their characterisation will then be transferred to SiPMs.

5.1.1 Signal shape of a SPAD

The ideal signal shape of a SPAD (cf. sec. 3.3) can be divided into three parts: before photons are detected, there is no current flowing; then, the photon impinges and creates *eh*-pairs, leading to an exponential increase of the current; finally, after the quenching occurs, the avalanche stops and the current decays exponentially. An example is shown in fig. 5.1.

The current of the rising edge $i_{rise}(t)$ of the signal (from t_i to t_{max}) can be modelled with an exponential function depending on the resistance R_S and the capacity C_J of a SPAD analogous to a capacitor:

$$i_{rise}(t) \propto 1 - e^{-\frac{t}{R_S C_J}} \quad (5.1)$$

Likewise, the current of the falling edge $i_{decay}(t)$ of the signal (from t_{max} to the end of the signal) can be described as an exponential (where R_Q is the quenching resistance):

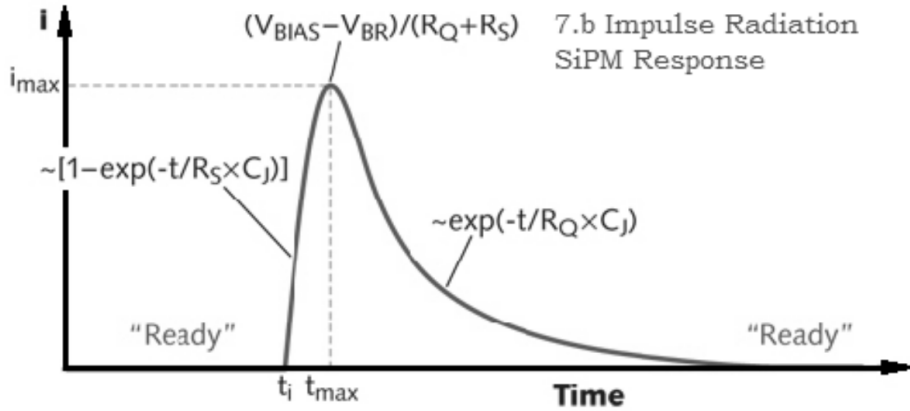


Figure 5.1: Typical signal form of a SiPM or a single SPAD. The current over time is plotted. The SiPM is “ready”, which means it is able to detect a photon. After the avalanche starts, the current increases exponentially, depending on the resistance R_S and the capacity C_J . As the quenching sets in, the peak of the signal is reached. The height of the peak is given by eq. 5.3 (here, voltages are labelled V instead of U). After the avalanche has ended, the current decays exponentially and the SiPM is “ready” again. Figure taken from [12]

$$i_{decay}(t) \propto e^{-\frac{t}{R_Q C_J}} \quad (5.2)$$

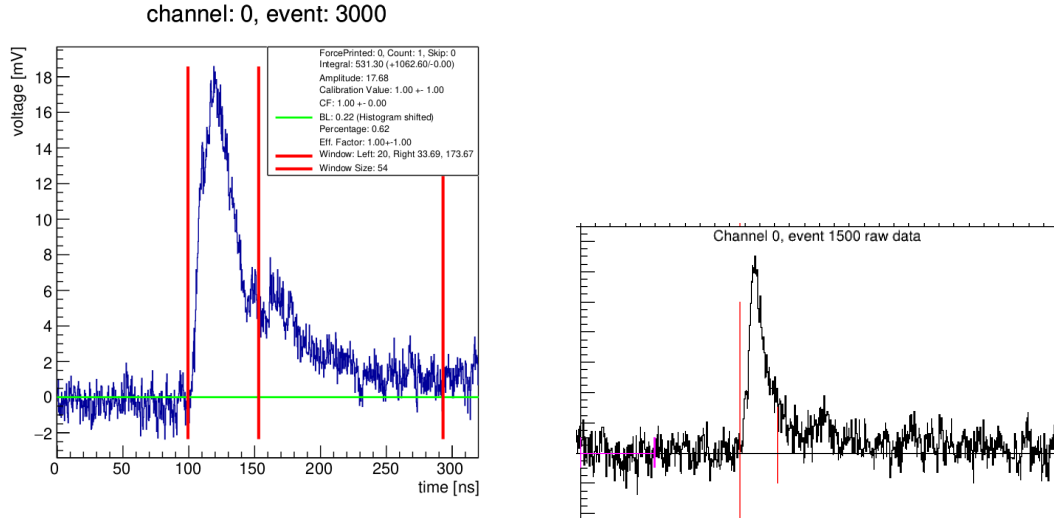
The maximum photocurrent i_{max} is given by [12]

$$i_{max}(t_{max}) = \frac{U_{bias} - U_{breakdown}}{R_Q + R_S} \quad (5.3)$$

As mentioned above, the parallel connection of the SPADs to a SiPM lead to the output of a single peak (cf. sec. 3.3), so that several SPAD signals overlap. Hence, it is a question whether this mathematical model still holds. To assess this, the difference in the incidence times of the photons is of importance.

5.1.2 Signal shape of a SiPM

The usual width of the SiPM signal is $\mathcal{O}(10 \text{ ns})$. If the difference in photon arrival time is significantly smaller, one can neglect the difference of the arrival time and the output signal behaves according to eq. 5.1 and 5.2, as is shown in fig. 5.1. More specifically, the peak height for the detection of two photons equals the superposition of two single photon peaks. The same is true for the charge, which is the time integral over the current. The assumption that the arrival time difference is smaller than the signal width is reasonable for



(a) Single event waveform created by the RootReader. The blue line indicates the measured values and the green line the calculated baseline (cf. sec. 5.3); the measured values have been shifted so that the baseline lies at 0 mV. The integral borders are marked by the left-most and central solid red lines and the right-most red line shows the estimated period of three afterpulse oscillations.

(b) Single event waveform created by the WaveCatcher Analysis. The black line indicates the measured values. The pink line shows the area where the baseline was determined; the measured values have been shifted so that the baseline lies at 0 mV. The integral borders are marked by the solid red lines.

Figure 5.2: Examples of a single event waveform, in this case from a measurement with the laser setup.

calibration measurements, where a picosecond laser is used (cf. sec. 4.3 and sec. 5.7.1).

If the photon arrival times are in the same order as the width, the resulting signal shape is different from the one of a single SPAD; it gets broader. The relation that the charge is the time integral over the photocurrent still holds.

5.1.3 Noise and electronic influences

A single event waveform can be divided into three parts: the *signal-free region before the signal*, which in fig. 5.2 can be identified with the region left of the red line, the *signal*, which is located between the two red lines on the left and the *region after the signal*, which is the region right of the second red line. The meaning of the third red line in fig. 5.2a will be explained later.

Ideally, the signal free region should only show entries at 0 mV, but mainly electronic noise leads to oscillations around 0 mV. The average over time of

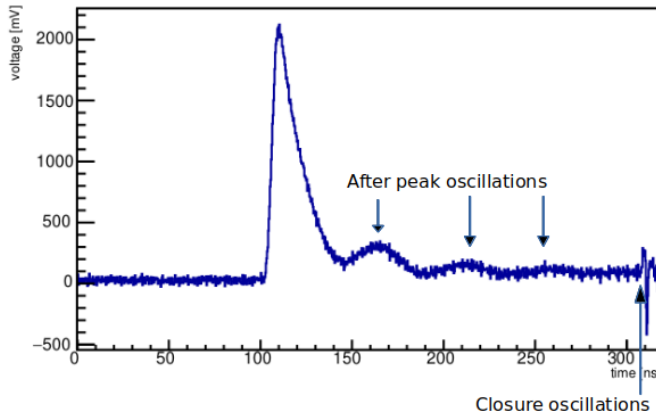


Figure 5.3: Sum of all waveforms in channel 0 for a measurement with the laser setup. After peak oscillations, nano oscillations and closure oscillations are visible.

these oscillations is not necessarily 0 mV. This offset, the *baseline*, needs to be accounted for. The determination of the baseline in the signal analysis is explained in sec. 5.3.

In an ideal scenario, the signal is the first peak in time in the waveform. Dark counts can of course occur at any time, so that they can also form the first peak in time.

With a perfect setup, one would only see one peak per photons that arrive simultaneously, after which a region that looks like the pre-peak region followed. In both setups however, so-called **after-peak oscillations (APO)** occurred (cf. e. g. [32]). They can likely be explained by the different impedances of the MCX cables and the WaveCatcher, which cause a part of the electronic signal to be reflected back into the cable. The reflected signal travels across the cable, gets reflected again at the other end and then detected with a certain delay compared to the original signal, where reflection at the MCX to WaveCatcher crossing happens several times. As the cable length is in the order of $\mathcal{O}(3 \text{ m})$ and the speed of light in the cable is around 20 cm/ns [21], the period of the APOs should then be in the order of $\mathcal{O}(50 \text{ ns})$. Furthermore, if the MCX cables are shortened, the period of the APOs is reduced [25]. For single event waveforms, APOs are not visible due to other noise and the falling edge of the signal, but they are clearly visible in the sum histogram where all events per channel are summed, cf. fig. 5.3.

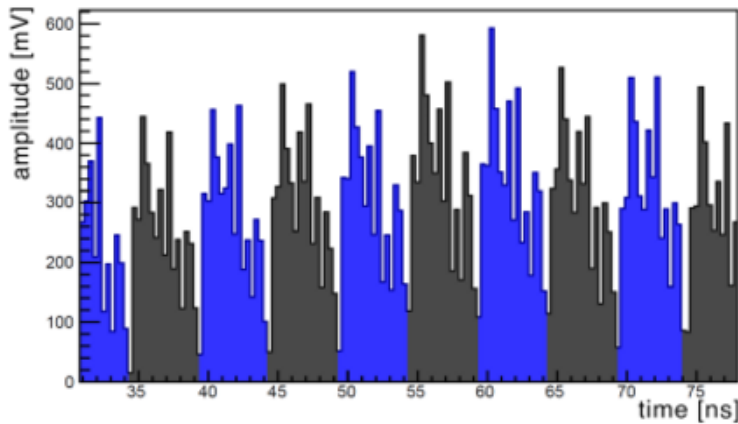
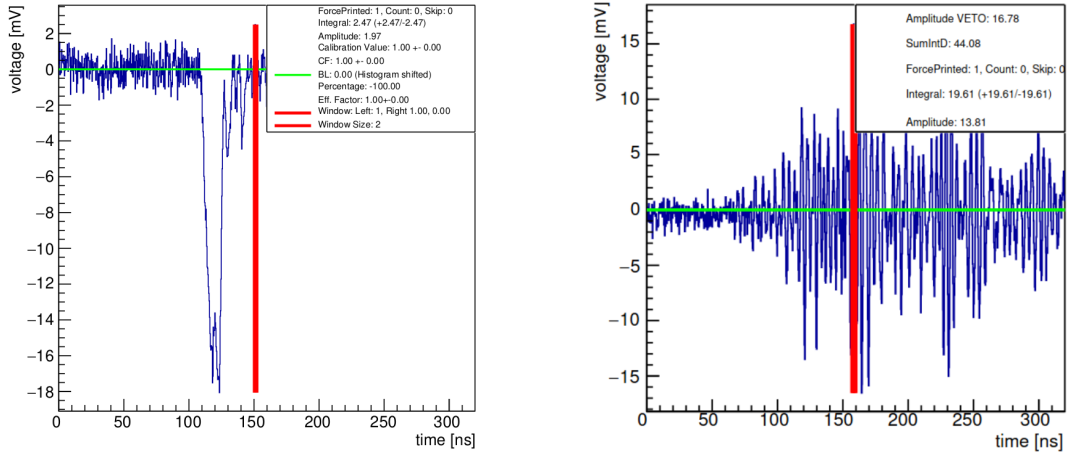


Figure 5.4: Zoomed in part of the sum of all waveforms of one channel. The colouring is only to illustrate the period of these oscillations. Figure taken from [32]

Another effect that can also be seen in fig. 5.3 are the so-called **closure oscillations**. They are a sudden voltage drop at about 310 ns followed by damped oscillations with a period of a few ns. The exact cause remains unknown, but speculations have been made that the WaveCatcher is the reason. This effect only becomes visible when adding up many events, as for single events, it remains invisible (cf. fig. 5.2). One could test this by comparing the signals measured with a PMT. The part of the event is not of interest for any part of this work anyway, so these oscillations can be disregarded.

A third kind of noise is introduced by the so-called **nano oscillations**. They come about through the layout of the memory chips in the WaveCatcher: they are subdivided into memory blocks that are arranged in 16 lines and 64 columns [22] plus a buffer. The voltage offsets of the buffers can be corrected in the WaveCatcher software. This was not done for this work, leading to small oscillations in the baseline (see also fig. 5.4) with a period of $\mathcal{O}(5\text{ ns})$. They can be effectively corrected by applying a smoothing algorithm to the waveform. In case of the RootReader, this is not done unless a peak finder algorithm is used, which is not the case for this work. In the WaveCatcher Analysis software, the smoothing is directly implemented.

Another kind of events caused noise: After a thunderstorm, there were events where the PMTs did not trigger on the characteristic voltage drop (fig. 5.5a), but rather a fast, decaying oscillation (fig. 5.5b). Meanwhile, the scintillator box readout did not register a signal apart from noise. These "weird" signals



(a) Usual waveform of a PMT channel for a muon event. The voltage drops steeply and slowly rises back to 0 mV.

(b) Unusual waveform of a PMT channel. The voltage oscillates rapidly and there is no signal in the liquid scintillator.

Figure 5.5: Comparison of the waveform in one trigger channel for a muon signal on the left and for an unusual event on the right. Events where the trigger signal looked like in fig. 5.5b were discarded by cutting on events where the voltage in a trigger channel exceeded 5 mV. The boxes in the corner give information about the integral window and the resulting integral value, the maximum amplitude and other values mostly needed for crosschecking.

occurred randomly over the course of a run, with $\mathcal{O}(50)$ of them being triggered when the light in the lab was switched on. The analysis thus neglected all events where the PMT voltage rose above 5 mV.

The analysis algorithm now has to determine the baseline, find a reasonable integration interval and produce an easily manageable collection of the results. In the next sections, the implementations of these requirements in the RootReader and the WaveCatcher Analysis will be discussed.

5.2 Conversion from raw data to .root file

As described in sec. 4.1.3, the raw digitized data from the WaveCatcher is stored in .bin files, where each bin file contains 1000 or 500 events. Each .bin file consists of the header, which contains information about the run and the version of the WaveCatcher software, and the actual data from the measurement. Each run has its own run number that is usually set when the measurement is started. To save memory and make the data more easily accessible and editable, all the .bin files of one run are converted into a so-called .root

file, which uses the ROOT software from CERN¹. .root files are organised like trees (hence the name): one dataset is called the tree, each branch represents one type of variable of the dataset and each leaf is a single value. Two different algorithms were developed: the **RootReader** by Jan Zimmermann² and the **WaveCatcher Analysis** by Dr. Christian Scharf³. The motivation for using two different algorithms is given in sec. 5.7.2. In this chapter, the steps of the data analysis will be explained and differences in the implementation between the two algorithms will be highlighted.

5.2.1 RootReader

The RootReader is a shell script that executes several C and C++ files. It is executed in the console either on Linux or a Windows subsystem for Linux. The user is presented with an interface in the terminal where he can enter a run number or a run number range, change several settings or start subroutines for the signal analysis⁴. The RootReader is able to handle several .bin files at once, where each one is opened in a separate thread. The individual data points are read out and stored along with several calculated values like the baseline and the integral (cf. sec. 5.3 and 5.4) in a .root file, where there is one .root file per .bin file at first. In the end, all single .root files are combined iteratively to form the resulting .root file. Additionally to the .root, three .pdf files are created: the waveform.pdf contains the waveforms of arbitrarily chosen events (usually every 1000th), the waveforms_chSum.pdf shows the sum of all event waveforms in each channel for a run and the waveforms_womSum.pdf shows the sum of all event waveforms of one run and one WOM (for this work, only one WOM was used, so in this case, it shows the sum of all waveforms of one run).

5.2.2 WaveCatcher Analysis

The WaveCatcher Analysis software is mostly written in C++. To execute it, the user has to run ROOT in the console and then execute the read.cc. The raw data .bin files are read out and the measured values can be stored in a

¹Download at <https://root.cern/install/>

²Download at <https://github.com/Uni2K/RootReader>, improved version with more functions at <https://github.com/andi-matter/bachelor/tree/andrea>

³Download at <https://github.com/cscharf-hub/wavecatcher-analysis>

⁴Download at <https://github.com/Uni2K/RootAnalysis>, further information in the wiki of the RootReader

.root file. Besides, .pdf files showing single event waveforms and the sum of all events per channel can be created.

5.3 Baseline determination

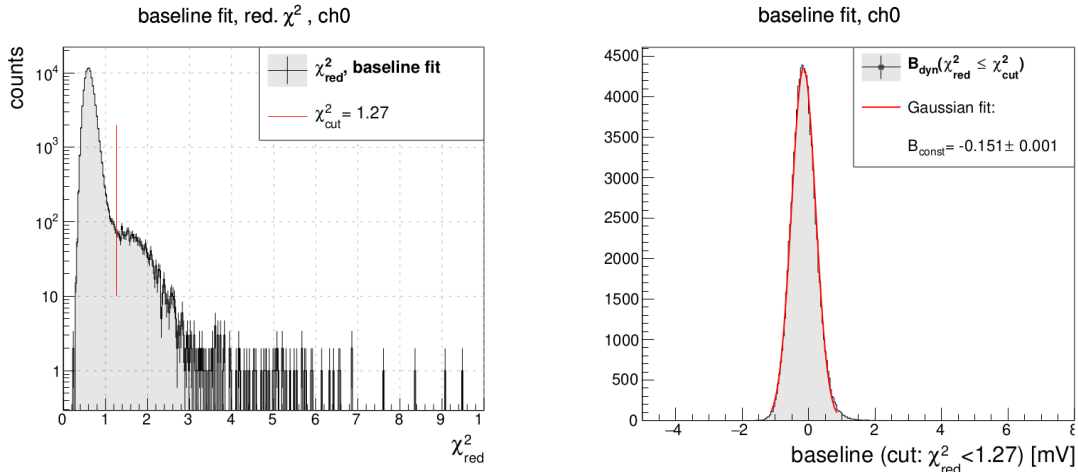
As mentioned in sec. 4.4, the region before the signal should ideally be at 0 mV. Due to noise, this is not true in the practical case, see e.g. fig. 5.2. If these fluctuations do not have an average value of 0 mV, this introduces a systematic error on the integral value. To minimize this error, the recorded voltage values are shifted by a constant B , called the *baseline*. Its determination is layed out in this chapter.

5.3.1 RootReader

In the RootReader, the baseline is calculated in two steps. First, the baseline of every single-event waveform is determined by fitting a constant fit with the parameter B to the first 30 ns of the event. The interval of 30 ns was chosen to assure that the beginning of the signal is not fitted. The trigger offset is chosen so that the signal starts at ≈ 100 ns. As there can be dark counts or electronic noise (especially for measurements without pole zero cancellation) in these 30 ns, it is possible to get a value that is much bigger than the actual offset in the signal region.

This is the reason to make the baseline determination event-independent. The idea is to discard all fits of dark count or noise events and calculate a baseline value from the remaining B values. If e.g. a dark count occured in the region where the baseline is determined, a constant fit is of course a bad fit model. To check how well the fit describes the data, the reduced χ^2 -value ($= \chi^2_{red}$), which is the χ^2 -value divided by the degrees of freedom of the fit, is calculated. A χ^2_{red} of 1 means a very good agreement of a constant fit to the data. To reject baseline fits where a constant fit is a bad assumption, a cut-off χ^2_{cut} value will be determined by the following procedure.

All χ^2_{red} -values are filled into a histogram, exemplary shown in fig. 5.6a. Usually, the distribution of the χ^2_{red} -values has a first clear peak at about $\chi^2 \approx 0.6$ and a second broader peak at higher values. The cut value χ^2_{cut} is chosen to be the minimum in between these two peaks; however, the maximum value of χ^2_{cut} is 1.27.



(a) Histogram of all χ^2_{red} -values of baseline fits of the events in channel 0. The red line indicates the value of χ^2_{cut} , which means that only the B -values that are associated to χ^2_{red} -values smaller than χ^2_{cut} are taken into account and filled into the B -histogram in fig. 5.6b.

(b) Histogram of all B -values that are related to χ^2_{red} -values smaller than or equal to χ^2_{cut} , denoted as $B(\chi^2_{red} \leq \chi^2_{cut})$ in channel 0. A Gaussian is fitted to this distribution and the mean \bar{B} is then used as the baseline value for channel 0 in the considered run for all events.

Figure 5.6: Demonstration of the process to determine the event-independent baseline (\bar{B}). The measurement is a calibration measurement using PCB D.

Only baseline fits with $\chi^2_{red} \leq \chi^2_{cut}$ are now used. Their B -values are filled into a second histogram, shown in fig. 5.6b. A Gaussian is fitted to this distribution. The mean value of the Gaussian \bar{B} is then used as the baseline value for all events in this channel for this run. All measured values are shifted by $-\bar{B}$ so that the average baseline (apart from dark counts) is considered to be 0 and the analysis continues.

5.3.2 WaveCatcher Analysis

In the WaveCatcher analysis, the baseline determination is not done event-independent. Instead, three options are given. In the most basic option, the algorithm calculates the mean voltage value in the first 50 bins, that is the first 16.25 ns, by

$$\bar{B}_1 = \frac{1}{t_2 - t_1} \int_{t_1}^{t_2} U(t) dt = \frac{1}{16.25 \text{ ns}} \int_{0 \text{ ns}}^{16.25 \text{ ns}} U(t) dt \quad (5.4)$$

This interval was chosen to make sure that no part of the signal is taken into account for the baseline. Henceforth, this will be called the *mean method* of

the baseline determination.

For the other two methods, the waveform is smoothed first. This is done by scanning the bins, calculating the mean over the neighboring bins and setting the new bin value to the mean. This means that for each bin i with the corresponding voltage $u(i)$, the new value $u_{\text{new}}(i)$ is given by

$$u_{\text{new}}(i) = \frac{1}{3} \cdot (u(i-1) + u(i) + u(i+1)) \quad (5.5)$$

The second method is based on the first method. Again, the average value over a 6.25 ns window is calculated by

$$\bar{B}_2(t_1) = \frac{1}{t_2 - t_1} \int_{t_1}^{t_2} U(t) dt = \frac{1}{6.25 \text{ ns}} \int_{t_1}^{t_1 + 6.25 \text{ ns}} U(t) dt \quad (5.6)$$

Different from the mean method, this is not done only once. Instead, the interval from 0 ns to 14 ns before the maximum value of the event is scanned. The starting time t_1 is iteratively set at each bin in this interval. As there are 45 bins in the 14 ns interval, 45 values for $\bar{B}_2(t_1)$ are calculated. Out of these 45 values, the minimum value is taken as the baseline correction \bar{B} . Therefore, this option is called the *minimal mean method*.

For the third option, the waveform is also smoothed first. Then, the slope of the waveform (Δy) over 6.25 ns is scanned in steps of three bin width ($\approx 1 \text{ ns}$) in the interval from 0 ns to 14 ns before the maximum value of the event. Then, one calculates

$$\xi(t_1) = \sum_{t=t_1}^{t=t_1 + 6.25 \text{ ns}} (\Delta y)^2 + \left(\sum_{t=t_1}^{t=t_1 + 6.25 \text{ ns}} \Delta y \right)^2$$

This gives a measure of the variation of the slope in the first term and the square of the integral over this interval in the second term for each t_1 . The idea is to look for the region where the slope varies only very little. The second term is needed to make sure that one does not choose a region where the variation of the slope is small because there is a trend in the data (e.g. the start of a signal). The second term would then become big. The smallest ξ -value is taken and the corresponding $t_{1,\min}$ is chosen as the start of the

integration window. Then the baseline correction is

$$\bar{B}_3(t_{1,\min}) = \frac{1}{t_2 - t_1} \int_{t_1}^{t_2} U(t) dt = \frac{1}{6.25 \text{ ns}} \int_{t_1}^{t_1 + 6.25 \text{ ns}} U(t) dt \quad (5.7)$$

This method is called the *minimal variation method*. It was employed in all studies using the WaveCatcher Analysis.

The difference in the baseline determination leads to different results, which was the main motivation to use both algorithms. For more details, see sec. 5.7.2.

5.4 Integration window determination

In order to determine the total charge that was created, one has to integrate over the signal. As discussed above, ideally, this would be very easy to do, because the signal would be the only region of the event where the voltage is not 0 mV. In reality, there are several kinds of noise before and after the signal. Therefore, the upper and lower integration border, from now on called the *integration window* have to be determined in a way that there is a balance between integrating as much as possible of the signal and as little as possible of the noise and that the ratio of the actual signal that is integrated remains constant. However, in the section 5.7.2, these claims will be relativised.

5.4.1 RootReader

As the trigger settings can vary as well as the exact incidence time of a photon on the SiPMs, one cannot integrate over the same interval for all events. Instead, the peak of the signal is used as a reference point⁵.

So, as a first step, the time of the maximum voltage t_{amp} is searched. To avoid integrating dark counts, this is only done in a fixed range, in this work between 100 ns and 200 ns. This also means that for events without any photo-electrons, a part of the baseline is integrated. As the integrated part contains the maximum voltage of the event (between 100 ns and 200 ns), this causes a

⁵Another possibility for a reference point one could use a constant fraction discrimination of the rising edge, e.g. where the signal first reaches the half of its maximum value. Although this generally is a bit less susceptible to statistical fluctuations, this method is not very reliable for low numbers of photo-electrons, as it is more likely to integrate dark counts or use their peaks instead of the signal peak

bias towards higher integral values when looking at all integral values.

The signal is not symmetrically shaped, therefore, the integration window is divided into two parts: the part left of the peak t_l , which covers the rising edge, and the part right of the peak t_r , which covers the falling edge of the signal up to the end of the integration window, see fig. 5.7. t_l and t_r indicate the time intervals from the time of the maximum, t_{amp} , instead of being the actual time where e. g. the integration starts. The value of the integral, called Λ , is calculated by

$$\Lambda = \int_{t_{amp}-t_l}^{t_{amp}+t_r} U(t) dt \quad (5.8)$$

Following [32], t_l has been chosen to be

$$t_l^c = 10 \text{ ns} \quad t_l^s = 20 \text{ ns}$$

The superscript c stands for (calibration) measurements done with the calibration setup and the superscript s means measurements with the cosmics setup. The different values are caused by different rise times of the signal in the two types of setups.

The choice of t_r takes into account that no APOs (cf. sec. 5.1) should be integrated. The integration should hence end at the low point between signal peak and first APO peak. This point is determined for each channel and for each run, like shown in fig. 5.7, by looking for said minimum in the sum histogram. The reason that the sum histogram is used is that the APOs are not always clear for single event waveforms, but are very easily visible for the sum of waveforms.

As described in further detail in sec. 5.7.2, for a big part of this work, an integration window of only 2 ns was used, with $t_l = t_r = 1 \text{ ns}$. To explain the reason for this, first, the pulse-charge spectrum has to be introduced.

5.5 Charge and gain

Now that the integration window has been determined, the physical meaning of the integral value will be discussed. The measured signal is a voltage

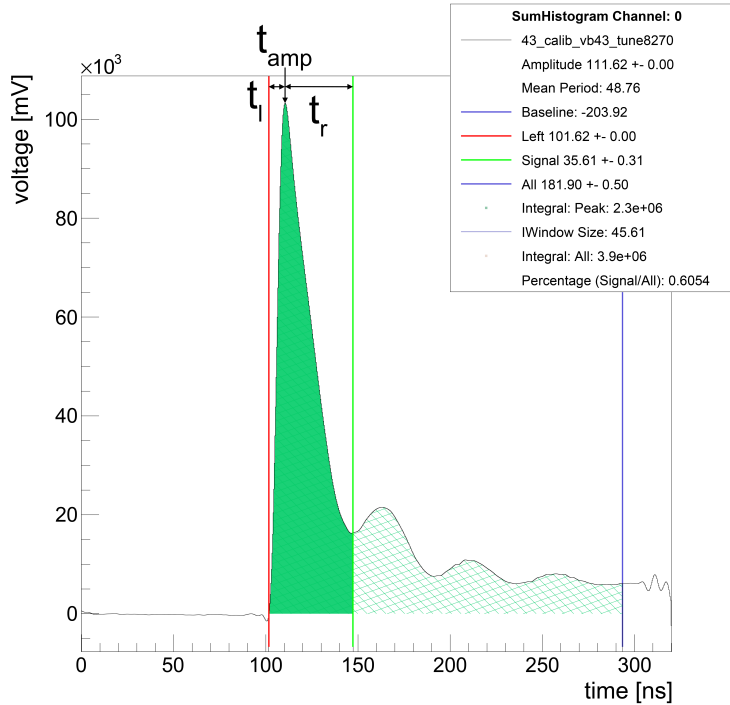


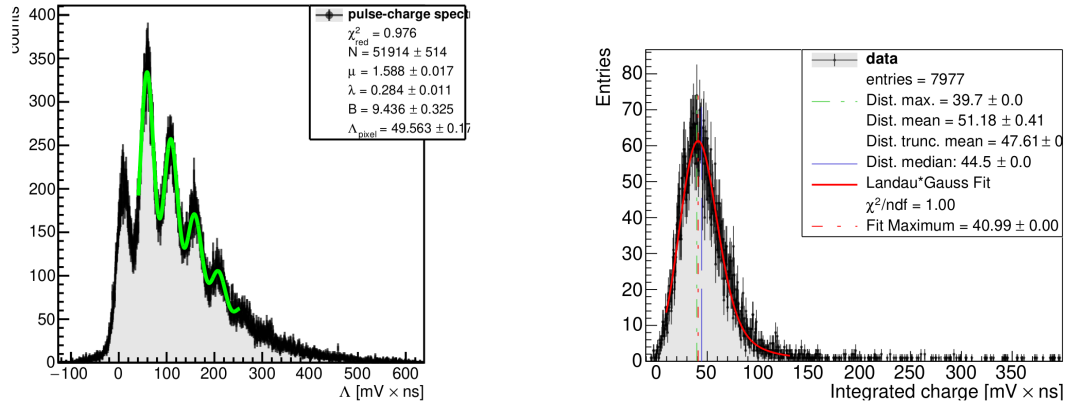
Figure 5.7: Exemplary sum of all waveforms in channel 0 of a calibration measurement. The signal peak, three APOs as well as closure oscillations (cf. sec. 5.1.3), are clearly visible. The red solid line indicates the start of the integration window, the green line its end. The green coloured area is the integrated signal area. The blue solid line shows the end of three APOs, so the green hatched area is the area of three APOs, which can be used to estimate the error of the integral value. In the box, several parameters are given for crosschecking. The amplitude denotes the maximum voltage value of the sum. Furthermore, the baseline, the starting time and the duration of the signal are given as well as some values mostly for debugging.

$U(t)$. By dividing $U(t)$ by the resistance R of a SiPM pixel, one can calculate the current over time in the pixel $I(t)$. Integrating this over the period of one discharge Δt yields the charge Q_{pixel} .

$$Q_{\text{pixel}} = \int_{\Delta t} I(t) dt = \frac{1}{R} \int_{\Delta t} U(t) dt \quad (5.9)$$

Q_{pixel} gives the amount of charge that was released in one pixel during an avalanche (cf. sec. 3.3), called a *Geiger discharge*. The *gain* is Q_{pixel} in units of elementary charge e . As the charge can be calculated similar to a capacitor by the overvoltage U_{over} and the capacitance C of the SiPM [3], the gain is given by

$$G = \frac{Q_{\text{pixel}}}{e} = \frac{C \cdot U_{\text{over}}}{e} \quad (5.10)$$



(a) Example of a PCS of a calibration run taken with PCB D. The green line shows the Poisson \times Gauss fit $f(\Lambda)$ given in eq. 5.14. The legend shows the fit parameters, including Λ_{pixel} .

(b) Example of a PCS of a cosmic run using the SBT single cell prototype. The solid red line shows the Landau-Gauss fit $f^{LG}(\Lambda)$ given in eq. 5.16. The legend shows the position of the maximum (dashed green line), the mean, the truncated mean (mean of charge values of less than 150 mV \times ns), the median (solid blue line) of the distribution and the most probable value, which is the maximum, of the fit (dashed red line).

Figure 5.8: Examples of PCS of a calibration and a cosmic measurement including the corresponding fits (cf. sec. 5.7), evaluated with the RootReader.

The gain allows to infer the number of triggered pixels from the measured data. If the number of photons is smaller than the number of pixels, one can assume that the number of triggered pixels is equal to the number of detected photons (cf. sec. 3.3).

5.6 The pulse-charge spectrum

The pulse-charge spectrum (PCS) is the histogram which contains all Q_{pixel} -values of one channel and of one run. Examples can be seen in fig. 5.8.

In theory, Q_{pixel} can only take discrete values depending on the number of detected photons N_{pe} , as each photon triggers a Geiger discharge in one of the pixels. Doubling the number of detected photons would double the measured value of Q_{pixel} . In the PCS of a calibration measurement, one would therefore only expect discrete δ -functions with a fixed distance in charge, where each peak corresponds to a certain number of detected photons. In reality, the peaks have a finite width, as there are electronic noise effects that broaden them. Each peak with $N_{pe} = k$ can be described by a Gaussian with

a finite width given by σ_k [25].

$$\sigma_k = \sqrt{\sigma_0^2 + k \cdot \sigma_1^2} \quad k = 2, 3, 4, \dots \quad (5.11)$$

σ_0 is the width of the pedestal peak, which contains all events where no photons have been detected, so that it is only integrated noise. The width of this peak therefore gives information about the noise created by the measurement setup. σ_1 is the width of the $N_{pe} = 1$ peak and contains information about the statistics of the Geiger discharge electrons.

5.6.1 Calibration value Λ_{pixel}

If the width given in eq. 5.11 is smaller than the distance between the peaks, one says that one can resolve single photo-electron (PE) peaks. This is the goal of the calibration measurements. The peaks are equidistant, except for the pedestal peak which contains all integrals that relate to $N_{pe} = 0$. An example of a PCS where the PE peaks can be resolved is shown in fig. 5.8a.

Studies of the SiPMs require the determination of the so-called *calibration value* or Λ_{pixel} . This value describes the distance of the PE peaks in the PCS is therefore in units of mV \times ns. Λ_{pixel} is proportional to the *gain* G of a SiPM. Λ_{pixel} allows to convert the results from other measurements to the number of detected PEs.

5.6.2 Light yield

To compare how much light was detected in different measurements, the so-called *light yield* is used. If the gain is known, one can e. g. use the number of detected photons. Metrics that are also used for comparison instead are the mean and the truncated mean of the PCS distribution as well as the mean value of a Landau \times Gauss fit to the distribution (cf. sec. 5.7).

5.7 Fitting of the pulse-charge spectrum

5.7.1 RootReader

The RootReader script itself does not automatically create the PCS. Instead, an additional script must be executed. This script opens the .root file that

was created by the RootReader and fills all saved integral values into a new histogram.

Calibration measurements

The goal of a calibration measurement is to determine the Λ_{pixel} value described in sec. 5.6. To evaluate calibration runs, the FitCharge.sh routine has to be executed. For the fit function of the PCS it is assumed that the number of detected photons is described by a Poisson distribution with the mean μ . The effects of afterpulses and delayed cross-talk are neglected. The probability of prompt crosstalk is assumed to be $1 - e^{-\lambda}$, where λ is the so-called branching parameter. The Poisson distribution altered by cross-talk is then

$$\text{GP}(k, \mu, \lambda) = \frac{\mu \cdot (\mu + k \cdot \lambda)^{k-1} \cdot e^{-(\mu+k \cdot \lambda)}}{k!} \quad (5.12)$$

This will serve as the envelope of the fit function. Each PE peak is then represented by a Gaussian with a width σ_k (cf. eq. 5.11):

$$\text{Gauss}(\Lambda, k, \Lambda_{\text{pixel}}, B, \sigma_k) = \frac{1}{\sqrt{2\pi\sigma_k^2}} \cdot e^{-\frac{(\Lambda - (k \cdot \Lambda_{\text{pixel}} + B))^2}{2\sigma_k^2}} \quad (5.13)$$

The parameter B describes the x-position of the pedestal peak which arises from events without any photo-electrons ($N_{pe} = 0$). The convolution of the envelope and the single peak fit function is added up for each peak k up to a maximum value k_{max} that is the number of the peaks that are fitted. When applied, a normalization constant $1/N$ is multiplied to the function:

$$f(\Lambda) = \frac{1}{N} \sum_{k=0}^{k_{max}} \text{GP}(k, \mu, \lambda) \cdot \text{Gauss}(\Lambda, k, \Lambda_{\text{pixel}}, B, \sigma_k) \quad (5.14)$$

Cosmics measurements

Using the RootReader, it is usually not possible to resolve individual PE peaks in a cosmics measurement. A typical PCS is shown in fig. 5.8b. Different fit functions have been tried: a Poisson fit, a Gaussian, a Landau distribution (eq. 5.15) and a convolution of Landau and Gauss function (eq. 5.16).

$$\text{Landau}(\Lambda) = \frac{1}{\pi} \int_0^\infty e^{-t \cdot \ln(t) - \Lambda t} \sin(\pi t) dt \quad (5.15)$$

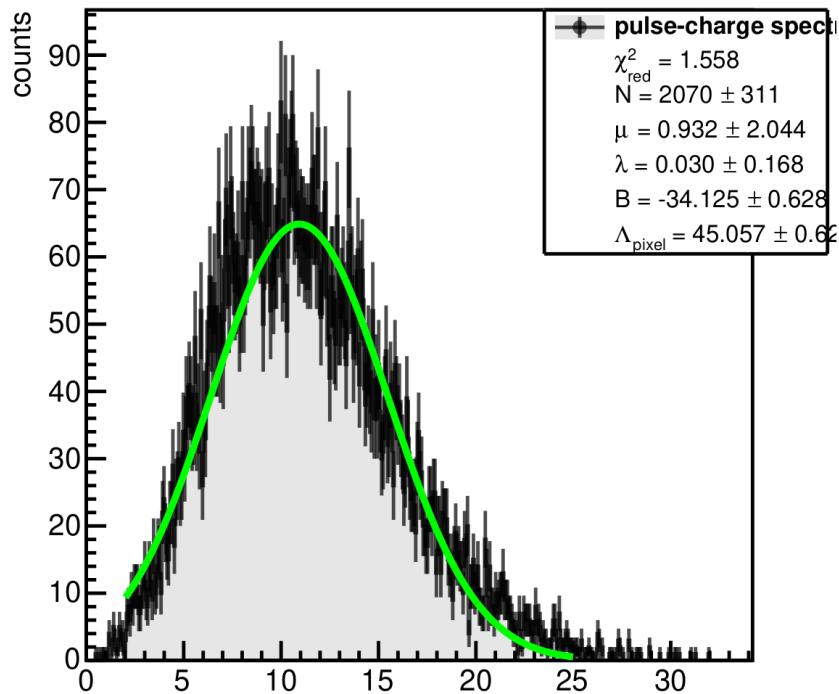
$$f^{LG}(\Lambda) = \text{Landau}(\Lambda) \cdot \text{Gauss}(\Lambda, k, \Lambda_{\text{pixel}}, B, \sigma_k) \quad (5.16)$$

For this work, the Landau-Gauss fit was used as it yielded good results and had the most physical plausibility: The Landau distribution describes the energy loss distribution by ionization of fast particles, which describes the excitation of the liquid scintillator by incoming charged particles. The most probable value (MPV) of the fit function, its maximum, is then taken as a measure for the light yield of the run and one channel.

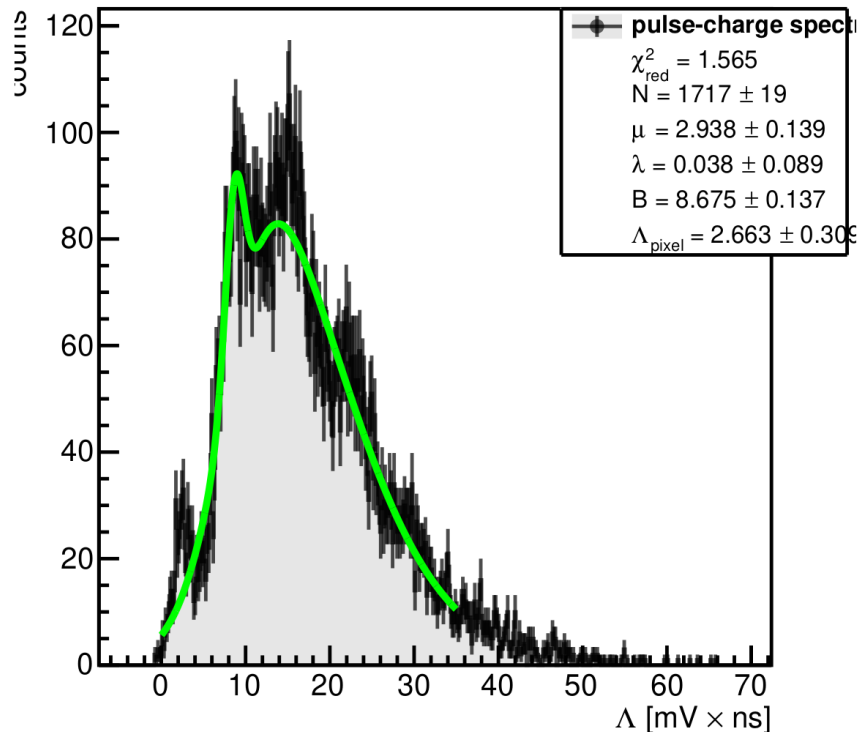
5.7.2 Motivation for the WaveCatcher Analysis

Obviously, the determination of Λ_{pixel} requires visible PE peaks in the PCS. While for measurements taken by [32], all SiPMs in a channel were switched on and PE peaks were clearly visible using PCB D (cf. fig. 5.8a), this changed for unknown reason for later measurements (cf. fig. 5.9a). A lot of different parameters have been varied to find the cause, including the overvoltage, different settings for the pole-zero cancellation and the number of SiPMs per channel that were switched on. In the end, calibration measurements for this work were taken at 3 V to 6 V overvoltage, without pole-zero cancellation and only one SiPM per channel switched on. In addition, the integration window of the RootReader was narrowed to ± 1 ns around the bin with the maximum value, so basically, only the amplitude was considered instead of the integral. With these parameters, individual photo-electron peaks could be resolved, but not as many and not as clearly as for previous measurements. An example for the resulting PCS using the RootReader is given in fig. 5.9b.

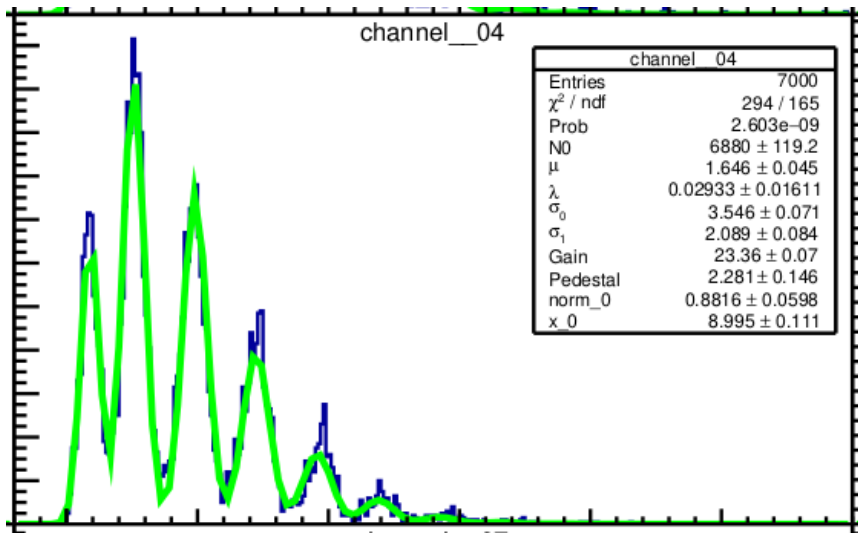
Only after the introduction of a new analysis code, the WaveCatcher Analysis, the PE peaks were clearly separated and the determination of Λ_{pixel} was possible with high enough precision (cf. fig. 5.9c). The integration window is also 2 ns centered at the maximum for the WaveCatcher Analysis, so the biggest difference between the two analysis methods is the baseline determination; therefore, this is very likely the reason for the difference in the ability to resolve the PE peaks. The fit function is the same as in the RootReader, see eq. 5.14.



(a) Example of a PCS of a calibration run with PCB J and an overvoltage of 3 V. No PE peaks are visible. The fit has no physical meaning in this case.



(b) Example of a PCS of a calibration run with PCB J and an overvoltage of 3 V analysed with the RootReader. PE peaks are visible, although not as clearly as in earlier studies (e.g. [32]). The fit has no physical meaning in this case.



(c) Example of a PCS of the same calibration run with PCB J as in fig. 5.9b and an overvoltage of 3 V analyzed with the WaveCatcher Analysis. PE peaks are visible.

Figure 5.9: Examples of PCS to clarify the motivation for the introduction of the WaveCatcher Analysis: For some unknown reason, the PCS of calibration measurements started showing no peaks anymore as e.g. in fig. 5.9a. Narrowing the integration window to 2 ns centered at the peak, measuring without pole-zero cancellation and with only one SiPM switched on per group yielded results as in fig. 5.9b. Introducing a new analysis algorithm, the WaveCatcher Analysis, with e.g. a new baseline determination (here, the minimal RMS method was used) and with smoothing of the waveforms, leads to significantly better results, shown in fig. 5.9c

6 Light yield comparison

6.1 Breakdown voltage

The breakdown voltage of the eight SiPMs that were used for the light yield measurements on the three PCBs was measured in short succession at 23.6 °C. The temperature fluctuations were smaller than 0.1 °C. To measure the breakdown voltage, only switch 1 was switched on in each channel. Then, the PCB was inserted into the laser setup and the WaveCatcher software was used in continuous mode, which means that the data was not stored, but monitored at the computer in real time. The laser tune was adjusted so that the signal reached maximum visibility; the chosen value was 72.80%. Afterwards, the voltage was lowered until no signal was visible apart from noise and dark counts. The voltage at which no signal can be seen was taken as the breakdown voltage $U_{\text{breakdown}}$. As mentioned in sec. 4.1.2, there is an offset of 891 mV between the voltage set on the voltage supply U_{set} and the actual voltage that is applied to the SiPMs U_{bias} , which means that $U_{\text{bias}} = U_{\text{set}} - 891 \text{ mV}$. In table 6.1, the results for $U_{\text{breakdown}}$ are shown, where $U_{\text{breakdown}}$ is equal to U_{bias} .

The PCBs C&D used SiPMs of the type S13360-3075PE. In the datasheet [13], their breakdown voltage is given as $U_{\text{breakdown,datasheet}} = 53 \pm 5 \text{ V}$ at 25°C, which is in good agreement with the measured values. PCB J used SiPMs of

ch	PCB C	PCB D	PCB J
0	51.7 V	52.3 V	37.1 V
1	51.8 V	52.5 V	37.2 V
2	51.7 V	52.4 V	37.2 V
3	51.9 V	52.3 V	37.4 V
4	51.9 V	52.2 V	37.3 V
5	51.7 V	52.3 V	37.3 V
6	51.9 V	52.4 V	37.4 V
7	51.8 V	52.4 V	37.2 V

Table 6.1: $U_{\text{breakdown}} (= U_{\text{set}} - 891 \text{ mV})$ values for the first SiPM in each channel on each PCB.

	PCB C	PCB D	PCB J
U_{bias} [V]	57.1	57.1	42.1
ch. 0	34.37 ± 0.08 mV · ns	28.82 ± 0.08 mV · ns	45.19 ± 0.12 mV · ns
ch. 1	32.22 ± 0.07 mV · ns	27.38 ± 0.07 mV · ns	43.85 ± 0.03 mV · ns
ch. 2	32.78 ± 0.07 mV · ns	27.85 ± 0.06 mV · ns	42.63 ± 0.04 mV · ns
ch. 3	30.02 ± 0.06 mV · ns	28.01 ± 0.05 mV · ns	43.03 ± 0.03 mV · ns
ch. 4	31.78 ± 0.07 mV · ns	31.20 ± 0.08 mV · ns	43.69 ± 0.01 mV · ns
ch. 5	30.34 ± 0.09 mV · ns	31.31 ± 0.09 mV · ns	43.91 ± 0.02 mV · ns
ch. 6	30.06 ± 0.08 mV · ns	30.58 ± 0.09 mV · ns	44.31 ± 0.18 mV · ns
ch. 7	31.25 ± 0.09 mV · ns	29.60 ± 0.09 mV · ns	44.61 ± 0.21 mV · ns

Table 6.2: Λ_{pixel} values for the individual channels of each PCB.

The errors are determined by the fit. These measurements were taken with one SiPM per channel (switch 1) and without pole-zero cancellation.

the type S14160-3050HS. Their breakdown voltage is given in [14] as $U_{\text{breakdown,datasheet}} = 38$ V. No confidence interval for the datasheet breakdown voltage was given.

6.2 Calibration results

Calibration measurements were taken for three PCBs, two of them, C&D, using S13360-3075PE SiPMs and PCB J using S14160-3050HS SiPMs, cf. table 4.1. The runs were recorded using only one SiPM per channel (switch 1) and without pole-zero cancellation. The temperature in the lab was 23 °C. Since a calibration measurement collecting 10000 events takes about two minutes, temperature variations during the run can be neglected. As the calibration measurements were recorded in short succession, the temperature difference between the runs is in the order of <0.1 °C. Thus, the results for Λ_{pixel} can be compared.

The integration window was chosen to be 2 ns. The Λ_{pixel} values were calculated using the WaveCatcher Analysis software, applying the minimal RMS method (cf. sec. 5.3.2). Due to these different settings, the resulting Λ_{pixel} values cannot be directly compared to previous results e. g. in [32], which used all SiPMs per channel, pole-zero cancellation and a different integration window (cf. sec. 5.4). In table 6.2, the calibration values Λ_{pixel} for each channel of each PCB, the bias voltage and the temperature are given. As previously stated in [32], the single channels do not show the same gain. This can be explained by different breakdown voltages of the single SiPMs.

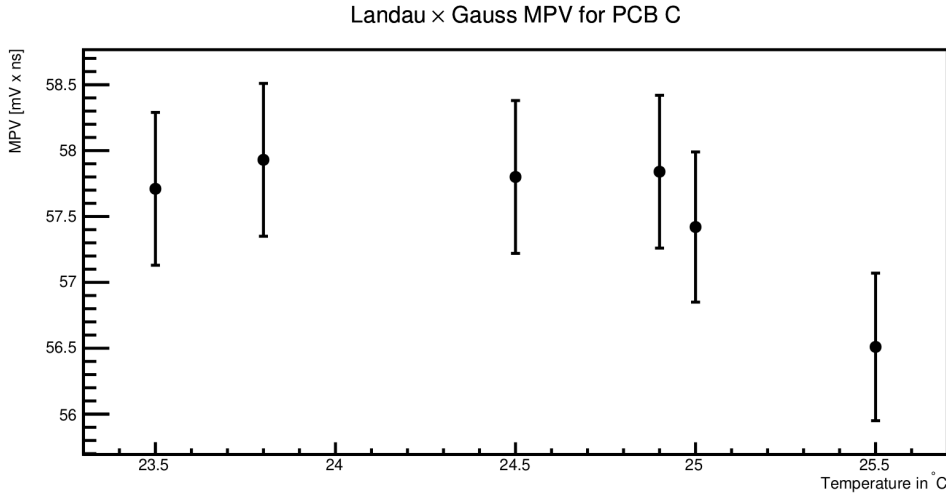


Figure 6.1: Light yield of six runs plotted over the average temperature of the corresponding run for PCB C. No correlation can be seen.

Although PCB C and D used the same SiPMs of the type S13360-3075PE, the Λ_{pixel} value of PCB C is 8% higher than Λ_{pixel} of PCB D for the same bias voltage. Their breakdown voltages differ by 0.6 V, meaning that the overvoltage U_{over} for PCB C has been 0.6 V higher as for PCB D at the same bias voltage. According to fig. 4.1, changing the overvoltage from 4.7 V to 5.3 V leads to an increase of the gain of roughly 10% (at 25°C), so the 8% higher Λ_{pixel} value is expected.

The gain is about 50 % higher for PCB J as for PCB C&D. As the latter have a pixel pitch of 75 μm and the former has a pixel pitch of 50 μm , the photon detection efficiency is about 10 % higher than for PCB J.

6.2.1 Temperature dependence

Over the course of the light yield measurements presented in sec. 6.3, the temperature varied between 21 °C and 26 °C. Over the course of a single measurements using the cosmics setup, which takes about eight hours, the temperature variation is in the order of 1 °C. To check whether the temperature has an influence in the same order of magnitude as the new optical coupling between each run, the MPV values of the Landau-Gauss fit are plotted over the average temperature during the run in fig. 6.1. While this figure shows only the results for PCB C, the plots for the other PCBs are in appendix A.

No correlation can be seen between the light yield and the temperature. Therefore, the temperature influence was neglected in comparison of the effect of new optical coupling between the runs in this work.

6.3 Light yield comparison between the PCBs

With each PCB (C, D and J), six measurements were taken with the setup described in sec. 4.2. For all runs, the plastic scintillators were in the L position, closest to the lab door. No pole-zero cancellation was applied and only one SiPM per channel (switch 1) was turned on to have the same conditions as for the calibration measurements. After each run, the PCB was removed, new optical gel was applied, and the PCB was reinstalled. This was necessary, because the WOM tube had to be removed from the scintillator box to glue the reflector onto it (cf. sec. 6.4). After removal, the PCB would have to be reinstalled and new optical gel would have to be applied. If this only happened once, this would introduce an unknown systematic error. By applying new optical gel after each run, one can estimate the error that the new optical coupling causes. However, only the PCB was removed and not the entire WOM tube. This still introduces a systematic uncertainty if the WOM assumes a different position in the PMMA vessel after the reinsertion than before. The WOM was not removed after each run because the spacer could easily fall off and block the PMMA vessel. As the new optical coupling of the WOM to the PCB introduces fluctuations in the light yield of up to 15%, the impact of the new position of the WOM tube can be disregarded.

The integration window was chosen to be 2 ns. As described in sec. 5.4 and 5.7, the integral values of one run and one channel were filled in a histogram and fitted by the convolution of a Landau function and a Gaussian. The most probable value (MPV) of the Landau-Gaussian fit is then used as a measure for the light yield. It is in units of mV·ns. Using the calibration value Λ_{pixel} , these MPV values can be converted to the most probable number of detected photons N_{PE} by dividing them by the Λ_{pixel} values given in table 6.2.

In fig. 6.2, the average number of detected photo-electrons N_{PE} per PCB is shown. The average was taken over all six measurements and the eight channels. The mean number of N_{PE} for PCB C is ≈ 2 , for D and J, it is a bit lower at ≈ 1.5 . The difference between PCB C and D can be explained by the difference in their breakdown voltage (cf. tab. 6.1).

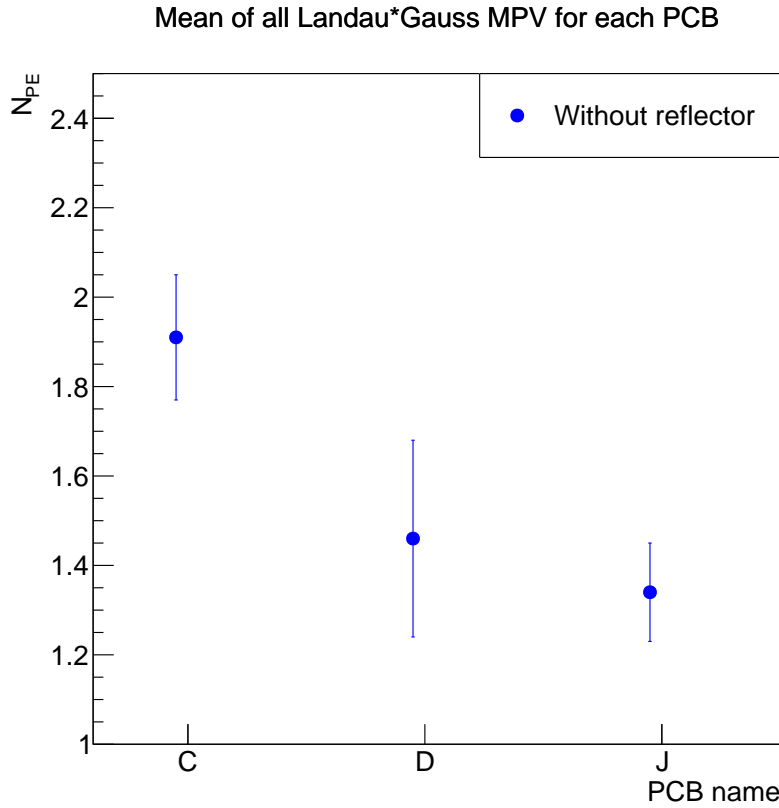


Figure 6.2: Average N_{PE} per PCB over six runs in all channels.

6.4 Light yield with and without reflector

A reflector was produced. It is made of high reflectivity aluminised mylar foil by AlFiPa [1]. It was cut by a printed circuit plotter, the ProtoMat H100 by LPKF [23], to match the 3 mm wall thickness of the WOM tube. Photos are shown in fig. 6.3. The ring was glued to the WOM tube using optical glue EJ-500 by Eljen Technologies. A heavy piece of metal was put on top of the WOM tube for 24 h to weigh the ring down and allow the glue to dry. Some irregularities can still be seen in fig. 6.3b, which might worsen the optical coupling of the WOM tube to the reflector and therefore decrease its reflectivity. After gluing the reflector ring to the WOM tube, it was reinserted into the setup. Again, six runs were recorded with each PCB.

The same integration window of 2 ns as without the reflector was used. In fig. 6.4, a comparison of the light yield channel by channel for each PCB can be seen. The measurements without the reflector glued to the WOM tube are shown as blue and purple circles, whereas the runs with the reflector are

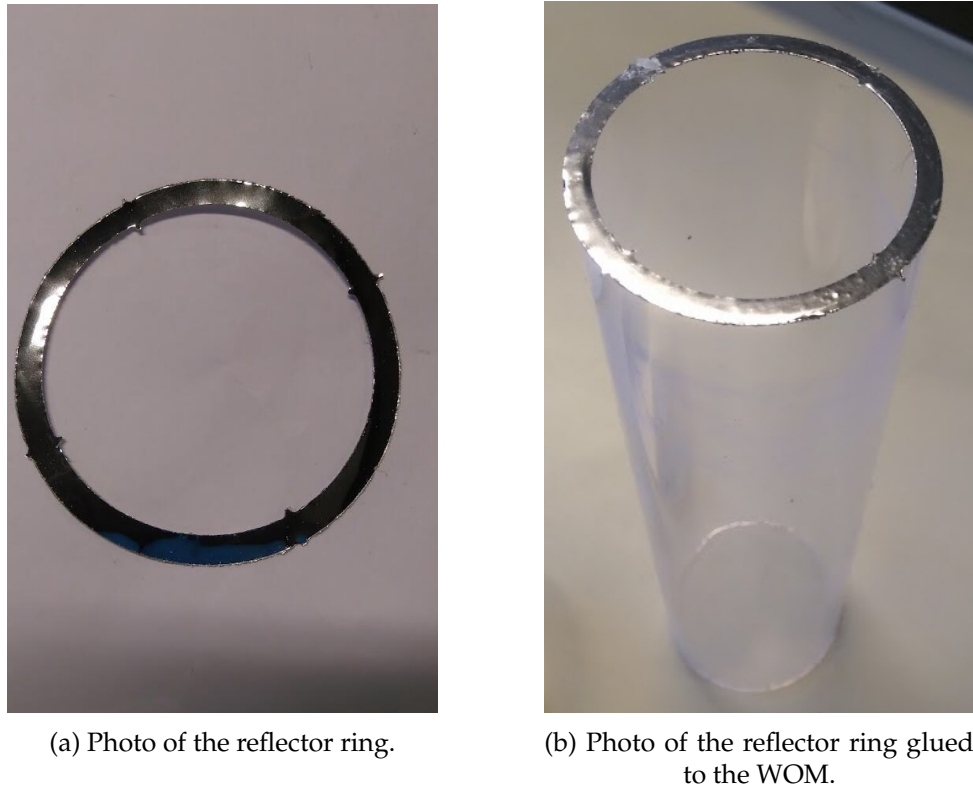


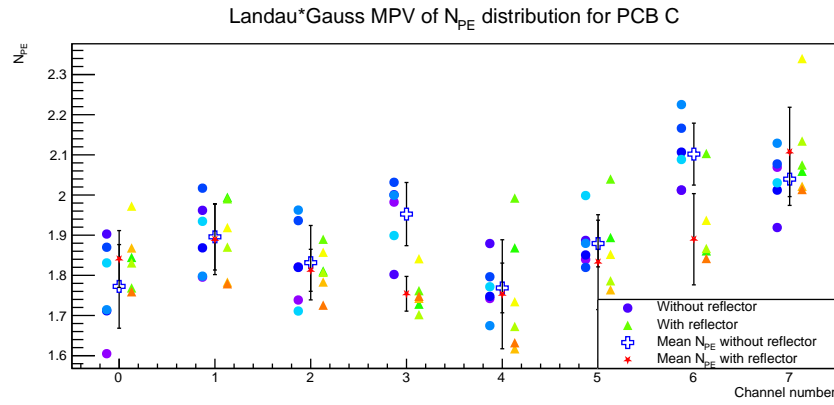
Figure 6.3: Photos of the reflector ring.

shown as green, yellow and orange triangles. N_{PE} is plotted over the channel number, with the results being shifted to the left and right a bit for better visibility.

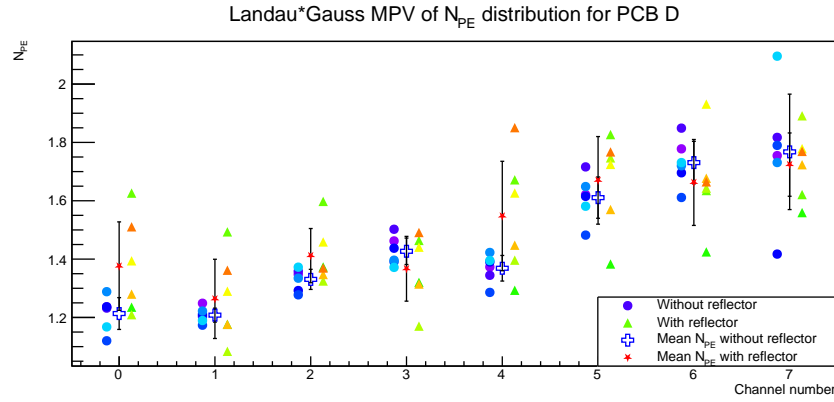
All values of N_{PE} are now averaged again over all channels and for all runs without reflector or with reflector for each PCB, resulting in one mean light yield without reflector (the same as in fig. 6.2) and one mean light yield without reflector per PCB. These values are shown in fig. 6.5.

For PCB C, the mean N_{PE} is in the order of one to two PE. There is no change in the light yield identifiable for the runs with the reflector. The same is true for PCB D, where the mean N_{PE} is ≈ 1.5 . For PCB J, the light yield with reflector is 14% higher than without, which is a change of 1.7 standard deviations. It is not clear why an improvement in light yield can be seen with PCB J, but not with the other two PCBs.

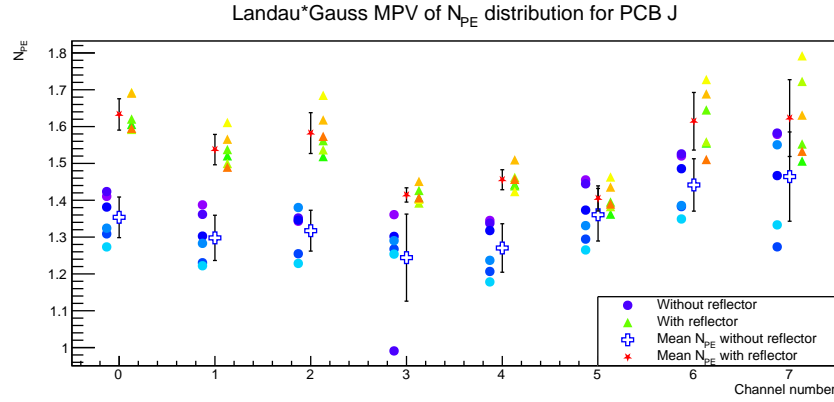
Three other measures of the light yield were used instead of the MPV of the Landau-Gauss fit: the mean value of the pulse-charge spectrum, the truncated mean value (only taking values below 150 mV·ns into account) and



(a) Comparison of the MPV value of the Landau-Gaussian fit to the N_{PE} distribution with and without reflector with the WOM coupled to PCB C.



(b) Comparison of the MPV value of the Landau-Gaussian fit to the N_{PE} distribution with and without reflector with the WOM coupled to PCB D.



(c) Comparison of the MPV value of the Landau-Gaussian fit to the N_{PE} distribution with and without reflector with the WOM coupled to PCB J.

Figure 6.4: Comparison of the light yield with and without the reflector. The values are shifted left and right from their actual channel number for better visibility. The cross shows the mean MPV value for each channel without reflector, the star indicates the mean MPV value per channel with reflector.

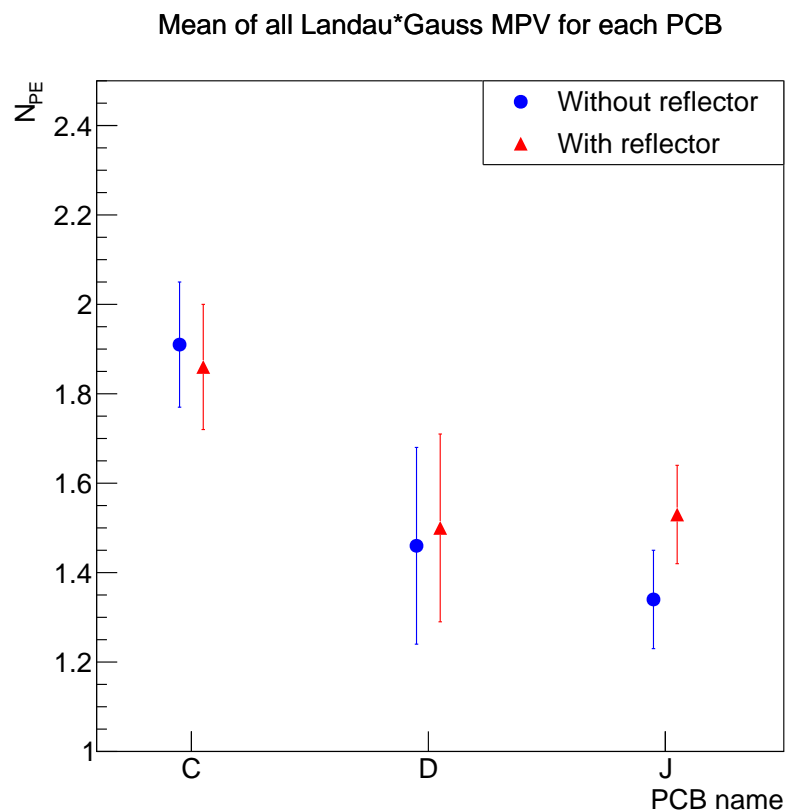


Figure 6.5: Average N_{PE} over all channels and all runs without reflector (blue dots) and with reflector (red triangles). The uncertainties are the standard deviation σ of the mean. Within 1σ , one cannot quantify a change in the light yield for PCB C and D. The change in light yield for PCB J is 1.7σ .

the median. The results show the same behaviour: The light yield does not change significantly for PCB C and D, but for PCB J, there is an increase. Thus, this cannot be explained by some bias in the fit, so that no conclusive statement on the improvement of the light yield due to the reflector can be made.

The removal and reinsertion of the WOM tube leads to a systematic uncertainty in the results. However, the WOM tube was not moved between the measurements with the reflector. Hence, if the WOM tube had a position that allowed for more or less light yield than before, this trend should be visible in all measurements after the reinsertion, so with the reflector.

6.5 Light yield with and without black foil at the end of the WOM tube

If the gluing of a reflector to the end of the WOM tube does not improve the light yield, this could mean that the light that reaches the end of the WOM tube is already totally reflected for the most part even without a reflector. To check this hypotheses, the reflector was removed using sandpaper, thus scratching the end of the WOM tube, and black foil was glued onto the end of the WOM tube. A photo can be seen in fig. 6.6. The expectation is that the light yield decreases significantly if the collected light at the SiPM array depends strongly on total reflection at the end of the tube.

Only PCB J was used. The same six runs without the reflector (cf. sec. 6.3) are used for comparison. After the gluing of the black foil, three runs were recorded. The results can be seen in fig. 6.7.

A clear decrease in light yield of around 30 % can be seen. Therefore, it is concluded that total reflection at the end of the WOM tube is an important process for the light detection of the SiPM array. A reflector does not lead to a large change, so that the border of PMMA to air already acts as a good reflector.

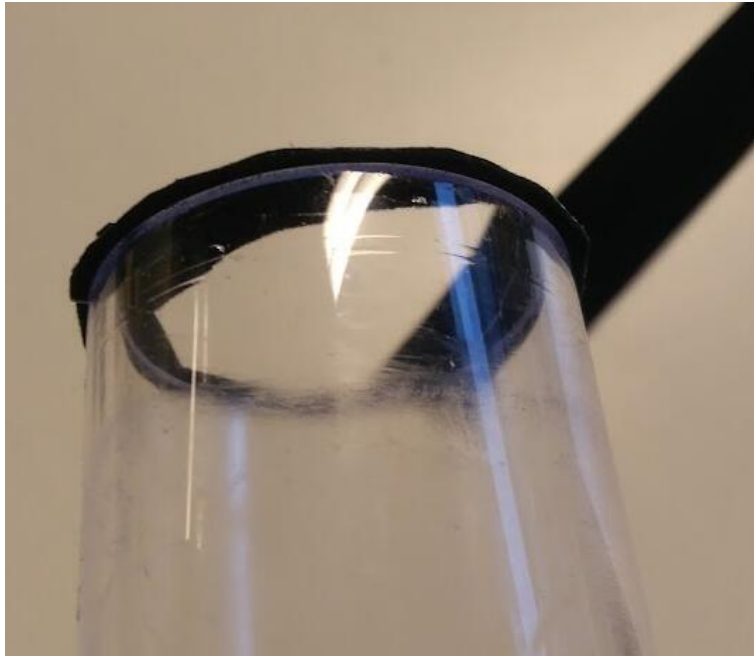


Figure 6.6: Picture of the black foil glued to the end of the WOM tube used to suppress reflection at the end of the WOM tube.

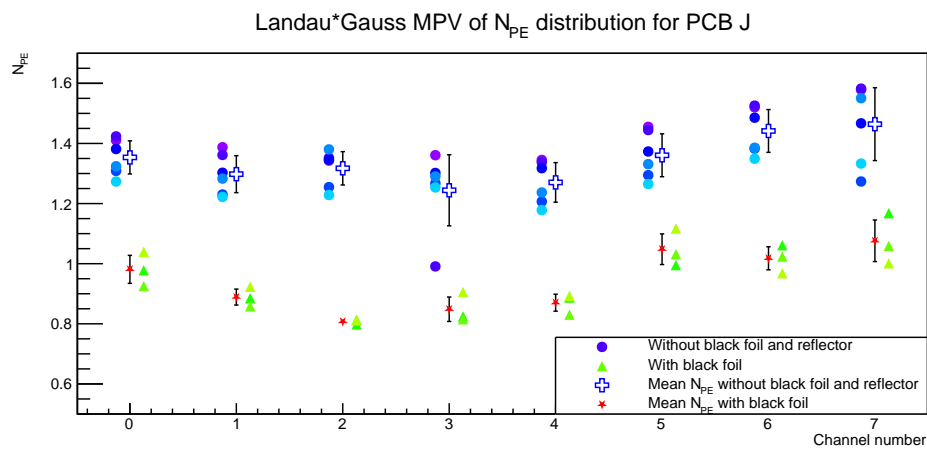


Figure 6.7: Comparison of the MPV value of the Landau-Gaussian fit to the N_{PE} distribution with and without black foil for the WOM coupled to PCB J.

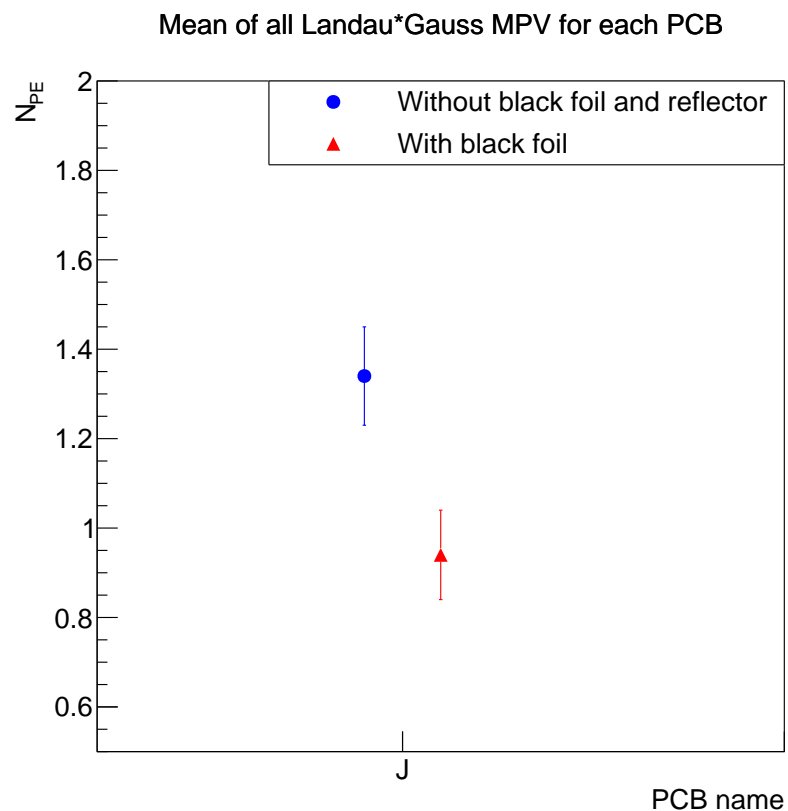


Figure 6.8: Average N_{PE} over all channels and all runs without reflector and black foil (blue dots) and with black foil glued to the end of the WOM tube (red triangles).

7 Reconstruction of the azimuth angle of a particle

7.1 Incidence position of muons

In this chapter, it is studied whether the measured data of the PCB can be used to determine the incidence position of the charged particle that crossed the cosmics box. Therefore, an independent way to determine the incidence position has to be implemented and the results from the PCB and the second, independent way have to be compared. As described in sec. 4.2, one plastic scintillator (PS) was installed above and below the scintillator box, respectively. At each end of the PS, photo-multiplier tubes (PMTs) were used to read out the PS scintillation light. Schematics can be seen in fig. 4.5. The trigger condition was that all four PMTs would record a voltage drop below -5 mV.

The PS can be moved in one dimension, allowing the selection of events where a muon crossed the box in the plane spanned by the two PS. For this work, they are always ordered vertically above each other. Three positions of the plastic scintillators were chosen: right (R), centre (C) and left (L)¹. They are shown in fig. 7.1.

By moving the PS, one can select muon crossing locations in one direction. To select events perpendicular to this direction, so along the PS, one has to filter the recorded signals by arrival times. The idea is that if a particle crosses a PS in the middle, scintillation light reaches both PMTs at (roughly) the same time. If a particle crosses the PS closer to one end though, the PMT on this end will record light earlier than the one on the other end. The refraction index of the PS is $n \approx 1.5$ [31]. The fact that the light is reflected very often inside the PS gives rise to an additional factor $f_{\text{refl}} \approx 0.75$ [10], so that the

¹Seen as standing in front of the setup with the window to the right.

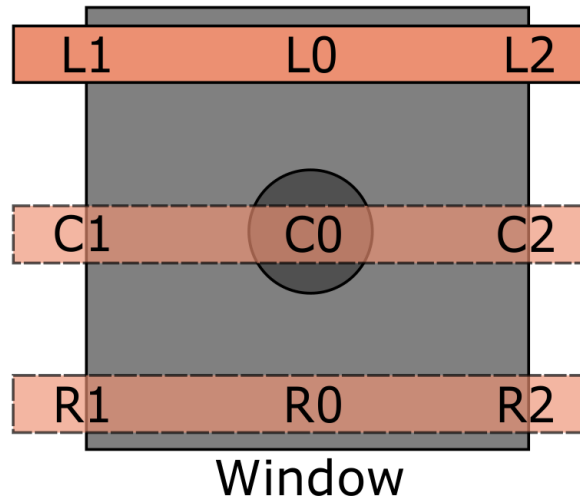


Figure 7.1: Sketch of the nine muon crossing locations in the scintillator box (light grey) and the WOM tube (dark grey) with respect to the lab window. The chosen positions of the plastic scintillators (shown in orange) are denoted by L, C and R. The plastic scintillator under the scintillation box is always located directly beneath the plastic scintillator above. The numbers 0, 1 and 2 denote the muon crossing locations filtered with time cuts. Figure taken from [10]

effective speed of light inside the PS can be written as

$$c_{PS} = \frac{1}{n} \cdot f_{\text{refl}} \cdot c_0 \approx 15 \frac{\text{cm}}{\text{ns}} \quad (7.1)$$

This can now be used to convert a time difference in the light detection in the PMTs to the distance from the centre of the PS where a particle crossed, called X. The starting times of a signal recorded in the PMTs are called t_a . They are determined via a constant fraction discrimination of 0.5 times the signal minimum (as the recorded voltage is negative), cf. fig. 7.2, which means that t_a is the time where the voltage first is 50 % of its minimum value. For the top PS, starting times of a signal are called t_1 and t_2 , for the bottom PS, they are t_3 and t_4 . Then the distance of the crossing particle to the centre of the PS is

$$X_{\text{top}} = \frac{1}{2} \cdot c_{PS} \cdot (t_2 - t_1) = \frac{1}{2} c_{PS} \cdot \Delta t_{21} \quad (7.2)$$

$$X_{\text{bot}} = \frac{1}{2} \cdot c_{PS} \cdot (t_4 - t_3) = \frac{1}{2} c_{PS} \cdot \Delta t_{43} \quad (7.3)$$

The convention is such that the centre point lays at $X = 0$, values $X < 0$ are to the left and values $X > 0$ are to the right of the centre. This gives rise to the factor of $\frac{1}{2}$. The time resolution of the PS is 1 ns [10], cf. sec. 7.1.1.

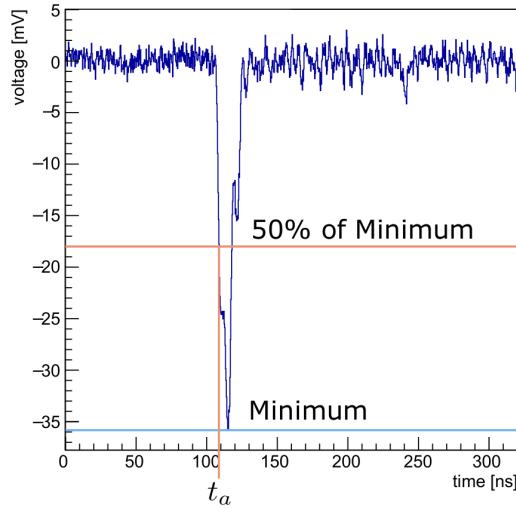


Figure 7.2: Illustration of the constant fraction discrimination. The minimum of the voltage is approximately -36 mV, so the arrival time is set to be where the voltage drops below the half of the minimum value, -18 mV. Figure taken from [10]

Using the positions X_{top} and X_{bot} , another plane of the muon incidence path is given. Three sections are defined similarly to the three positions of the PS, resulting in nine muon crossing locations. The letter indicates the physical position of the PS, whereas the number refers to the applied time cut. The time cuts for the nine muon crossing locations are given in table 7.1. The reason that the cuts are not symmetric is a difference of roughly 10 cm in the cable lengths from the PMTs on the right to the ones on the left. A top view onto the scintillator box with the nine muon crossing locations and the orientation of the PCB is shown in fig. 7.3. Based on the time cuts and the position of the box, each muon crossing location is assigned a muon incidence angle α viewed from the PCB. 0° points exactly to the corner of the box where R2 is situated.

7.1.1 Time resolution of the plastic scintillators

When looking at the distribution of measured values of Δt_{21} or Δt_{43} , one would expect its width to be determined by the length of the plastic scintillator $\Delta x = 57$ cm and the speed of light in the PS c_{PS} given in eq. 7.1 by

$$\Delta t = \frac{\Delta x}{c_{PS}} = 3.8 \text{ ns}$$

Position	Muon angle α ($^{\circ}$)	Δt_{21} (ns)	Δt_{43} (ns)
C0	–	[−1.75, 2.25]	[−1.15, 2.85]
L0	+135	[−1.75, 2.25]	[−1.15, 2.85]
R0	−45	[−1.75, 2.25]	[−1.15, 2.85]
C1	−135	> 6.25	> 6.85
L1	+175	> 6.25	> 6.85
R1	−85	> 6.25	> 6.85
C2	+45	< −5.75	< −5.15
L2	+95	< −5.75	< −5.15
R2	−5	< −5.75	< −5.15

Table 7.1: Assigned muon angle α and cuts on the time difference for each muon crossing location. The positions on the scintillator box are shown in fig. 7.3

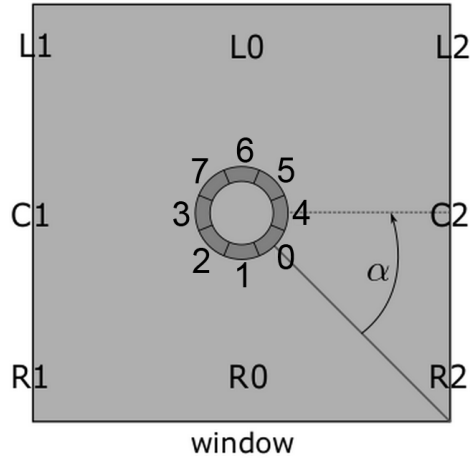


Figure 7.3: Sketch of the muon crossing locations shown on the top view of the scintillator box. The SiPM array sits in the middle of the box, at the C0 position. The channels are shown in the correct alignment to the scintillator box. Based on [10]

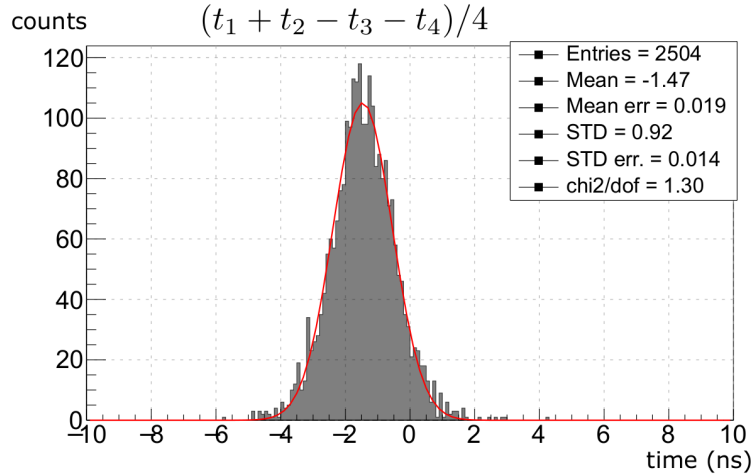


Figure 7.4: Distribution of the time of flight divided by 2, given by $(t_1 - t_3 + t_2 - t_4)/4$ for the position. The width of the Gaussian fit gives an estimate on the time resolution of the PMTs of 0.92 ± 0.01 . Figure taken from [10]

The time resolution can be estimated by only looking at particles that passed through the LS box on a path perpendicular to the plane of the PCB, so for each of the positions defined above [10]. As there are no diagonal paths, all path lengths and thus the times of flight should be roughly the same. The average time of flight from one PS to the other is given by

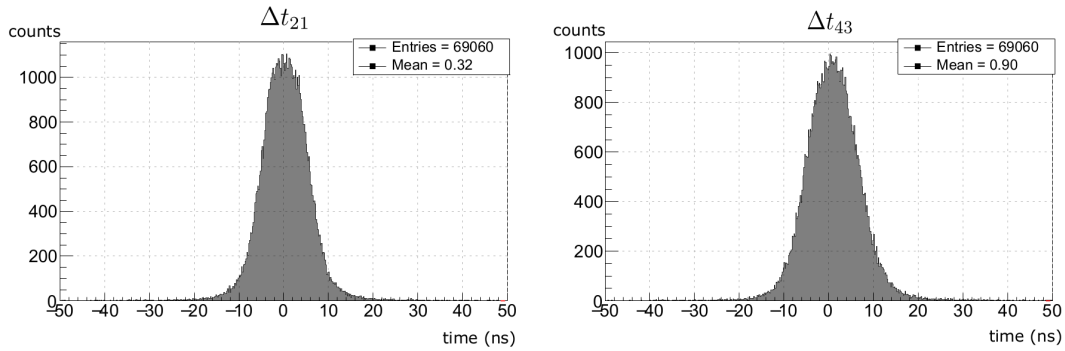
$$\frac{1}{2}(t_1 - t_3 + t_2 - t_4) \quad (7.4)$$

By calculating the distribution of the $(t_1 - t_3 + t_2 - t_4)/2$ values for all events in one position, one can estimate the time resolution of the PMTs. To have the same factor as the mean of all arrival times $(t_1 + t_2 + t_3 + t_4)/4$, the $(t_1 - t_3 + t_2 - t_4)/2$ distribution is divided by 2. The resulting $(t_1 - t_3 + t_2 - t_4)/4$ distribution is shown in fig. 7.4.

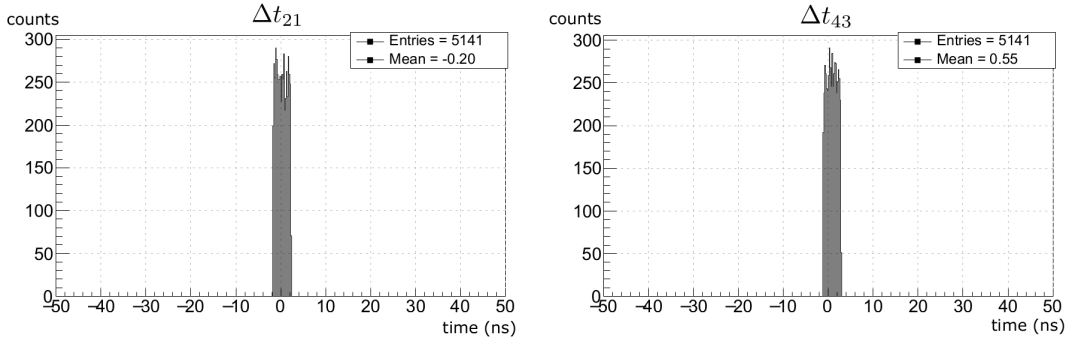
By fitting a Gaussian to the $(t_1 - t_3 + t_2 - t_4)/4$ distribution, the time resolution of the PMTs, which is given by the width of the Gaussian fit, was determined to be 1.0 ns [10]. This means that for the width of the Δt_{21} distribution, one would expect

$$\Delta t = \frac{\Delta x}{c_{PS}} = (3.8 \pm 1.0) \text{ ns}$$

However, the actual distributions of Δt_{21} and Δt_{43} in fig. 7.5a show a width of more than 10 ns. This effect is not fully understood. For the data analysis, the integral cuts were extended compared to those given by eq. 7.2 and eq.



(a) Histogram of the measured time differences in the PMTs Δt_{21} and Δt_{43} of a run with 69060 events. The width of the distribution is ≈ 12 ns. Figure taken from [10].



(b) Histogram of the measured time differences in the PMTs Δt_{21} and Δt_{43} of the same run as in fig. 7.5a with time cuts for the position R0 (cf. tab. 7.1) applied. The width of the distribution is now ≈ 2 ns. Figure taken from [10].

Figure 7.5: Time differences in the PMTs Δt_{21} and Δt_{43} without (fig. 7.5a) and with cuts (fig. 7.5b)

7.3 to keep a reasonable number of events.

7.2 Azimuth angle of a charged particle using the PCB

Now that an azimuth angle α is defined using the plastic scintillators (cf. fig. 7.3), the corresponding variable has to be introduced using the PCB. The mean azimuth angle of a charged particle with respect to the WOM tube and the PCB is named ϕ_{ew} (cf. [10], [16]). It is calculated as follows.

Each channel i on the PCB is assigned an angle φ_i . As there are eight channels and the PCB covers 360° , the spacing between these angles is $360^\circ/8 = 45^\circ$. In previous studies (e.g. [10]), it was assumed that the channels are numbered counter-clockwise, which of course lead to wrong results. For this work, one SiPM per channel was switched on to check to which channel in

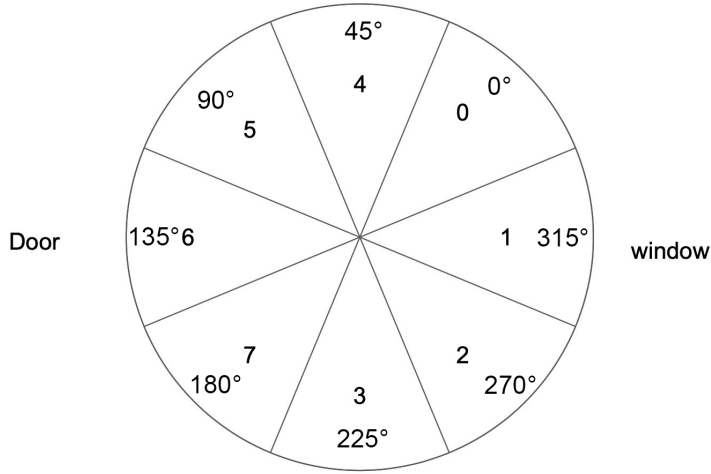


Figure 7.6: Sketch of the PCB with the channels i and their associated angles φ_i . The orientation in the lab is given by the indication of the window and door position. The orientation is rotated by 90° compared to fig. 7.3.

the WaveCatcher it actually corresponds. The ordering and the corresponding φ_i values can be seen in fig. 7.6.

In each channel, the light yield is called J_i . The light yield is used as a weighting factor. If one would only take the (weighted) mean of the angle values, this could lead to wrong results. For instance, if the same amount light comes only from 0° and 180° , the mean would be 90° , indicating that all light came from the channel with $\varphi_i = 90^\circ$, although there was no light detected at all in this channel.

The solution is to determine ϕ_{ew} via vectorial addition. One defines [10], [16]

$$x_i = \cos(\varphi_i) \cdot J_i \quad y_i = \sin(\varphi_i) \cdot J_i \quad (7.5)$$

$$X = \sum_{i=0}^7 x_i \quad Y = \sum_{i=0}^7 y_i \quad (7.6)$$

To retrieve an angle for one event, the final step is

$$\phi_{ew} = \arctan\left(\frac{Y}{X}\right) \quad (7.7)$$

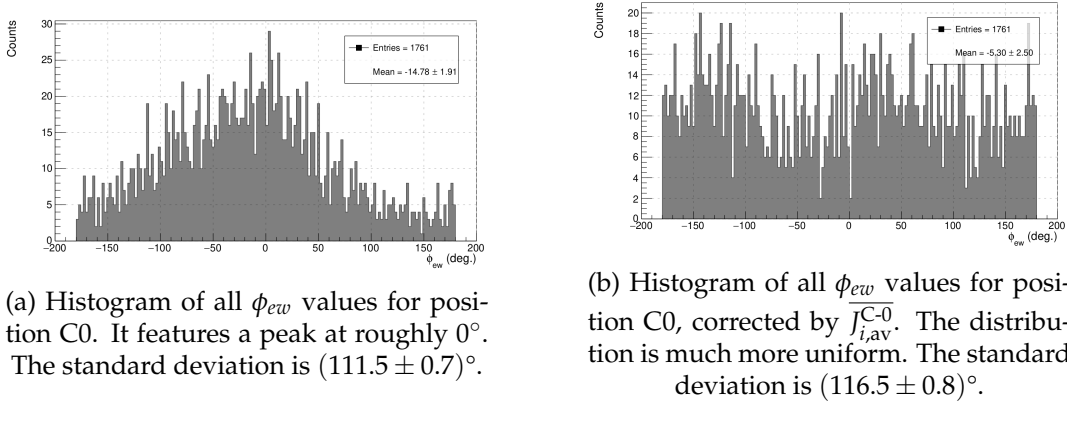


Figure 7.7: Histograms of the ϕ_{ew} values of position C0 with and without correction.

7.2.1 Correction of the ϕ_{ew} value

When all ϕ_{ew} values of the C0 position are filled in a histogram, one would expect a uniform distribution over the entire 360° , because when one measures at the centre of the box, each azimuth angle of an incoming particle is equally probable. However, as shown in fig. 7.7a, the distribution is not uniform, but features a bias towards 0° . This can be explained by non-ideal optical coupling, due to non-uniform distribution of optical gel, non-ideal overlap between the SiPM array and the end of the WOM tube or different SiPM efficiencies. To account for this effect, every light yield value of channel i in each position was divided by the average light yield in the same channel for the C0 position $\overline{J_{i,\text{av}}^{\text{C-0}}}$. The J_i from eq. 7.5 are therefore substituted by \overline{J}_i

$$J_i \longrightarrow \overline{J}_i = \frac{J_i}{\overline{J}_{i,\text{av}}^{\text{C-0}}} \quad \overline{J}_{i,\text{av}}^{\text{C-0}} = \frac{J_{i,\text{av}}^{\text{C0}}}{\frac{1}{8} \sum_{k=0}^7 J_{k,\text{av}}^{\text{C0}}} \quad (7.8)$$

After calculating ϕ_{ew} using the \overline{J}_i values given in eq. 7.8, the distribution is more uniform, as shown in fig. 7.7b. This is the wanted effect, because one would expect a uniform distribution as argued above.

7.2.2 Event-independent mean angle $\overline{\phi_{ew}}$

With the normalised light yields in eq. 7.8 and the vectorial addition given by eq. 7.5 and 7.6, one can determine the azimuth angle of a particle for a single event ϕ_{ew} by eq. 7.7. In this section, the goal is to define an event-independent mean azimuth angle $\overline{\phi_{ew}}$ which describes the mean azimuth angle with respect to the WOM tube and the PCB for one run with one muon

crossing location as defined by tab. 7.1. For each of the eight positions (C0 excluded) the ϕ_{ew} values are filled in a histogram and a Gaussian is fitted to the distribution to obtain the event-independent azimuth angle $\overline{\phi_{ew}}$. In order to not introduce a bias in the fit concerning the position of the peak, the periodicity of the ϕ_{ew} values is used: The original ϕ_{ew} values are plotted as well as the values shifted by $\pm 360^\circ$. Then, a triple Gaussian (eq. 7.9) is fitted to the resulting three peaks, shown in fig. 7.8.

$$f_{3G} = p_0 \cdot \sum_{i=-1}^1 \exp \left[-\frac{1}{2} \left(\frac{x - p_1 + i \cdot 360}{p_2} \right)^2 \right] + p_3 \quad (7.9)$$

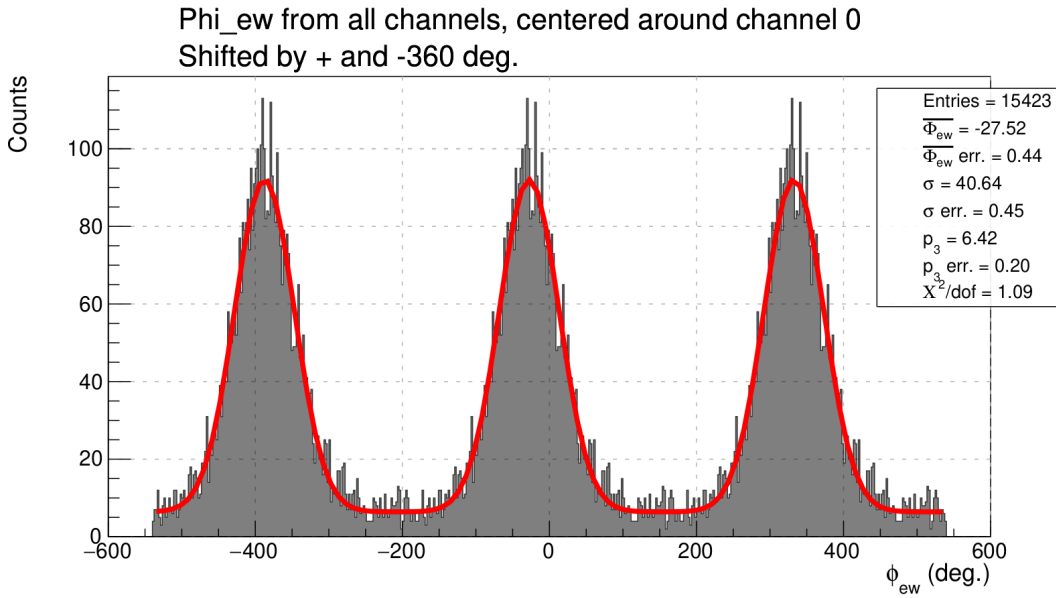
The mean angle $\overline{\phi_{ew}}$ is now fitted as parameter p_1 with a standard deviation of $\sigma = p_2$. p_0 is used for normalization and p_3 is the offset from 0, but both parameters are not further analysed. As α and $\overline{\phi_{ew}}$ both measure the azimuth angle of a charged particle crossing the scintillator box, they should have a linear correlation.

7.3 Directional reconstruction

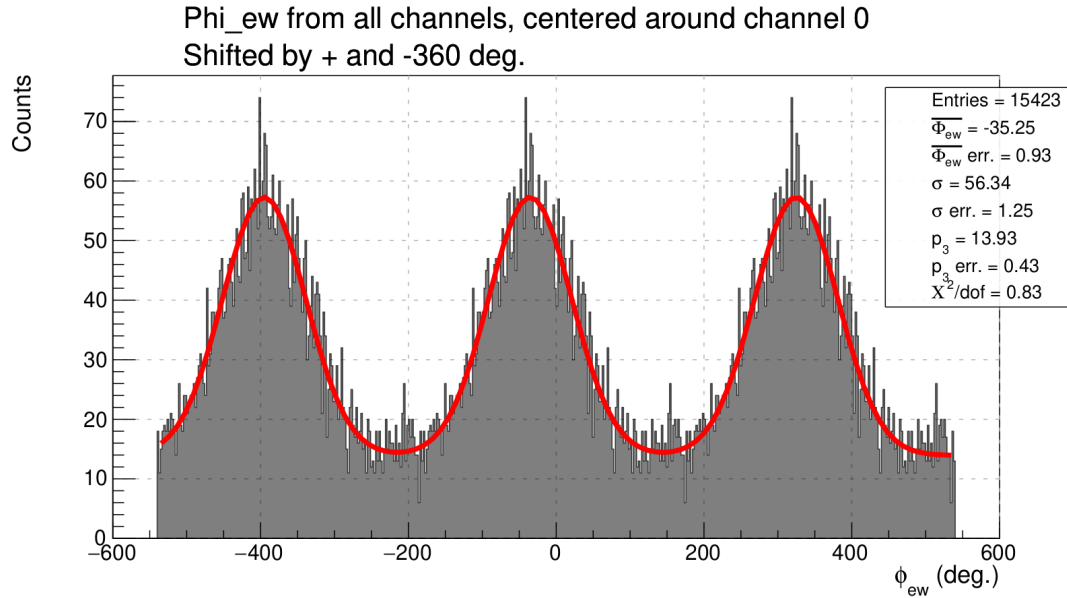
As described in sec. 7.2, for each event, a mean incidence angle ϕ_{ew} and a mean angle of an entire run $\overline{\phi_{ew}}$ are calculated. Several runs with 70 000 to 90 000 events each have been recorded over the course of a few days and evaluated in [10]. They are grouped by the three positions of the plastic scintillators (R, C, L) and three different time cuts (0, 1, 2, cf. tab. 7.1). As discussed in [10], the temperature fluctuations during the runs were between 0.4° C to 0.7° C. Their effect on the light yield can therefore be neglected.

For each position, except C0, the $\overline{\phi_{ew}}$ -value was calculated. When plotting the $\overline{\phi_{ew}}$ -values over the corresponding α -values, a linear dependence can be expected. The plot is shown in fig. 7.9. The linear regression shows a slope of $n = (0.96 \pm 0.04)$. For a single event, one can identify the azimuth angle of the particle with an accuracy of $\pm 46^\circ$ at the 1σ -level. This means that at the 2σ -level, one can infer the half of the PCB on whose side the particle crossed the detector box.

This result is in contradiction to earlier studies, cf. [10]. The reason is that the numbering of the channels was wrong in these studies: instead of just being numbered counter-clockwise, the numbering is as shown in fig. 7.6, as found



(a) Histogram of the original ϕ_{ew} distribution without the correction described in sec. 7.2.1. The values are also shifted by $\pm 360^\circ$. A triple Gaussian given in eq. 7.9 is fitted and the event-independent mean angle $\overline{\phi_{ew}}$ is obtained.



(b) Histogram of the original ϕ_{ew} distribution with the correction described in sec. 7.2.1. A triple Gaussian given in eq. 7.9 is fitted and the event-independent mean angle $\overline{\phi_{ew}}$ is obtained.

Figure 7.8: Histograms of the single-event ϕ_{ew} values, without (fig. 7.8a) and with (fig. 7.8b) correction. The values are also shifted by $\pm 360^\circ$, to ensure that there is no bias in the peak position parameter. The number of events is 15423. The value of $\overline{\phi_{ew}}$ is shifted and the standard deviation increases when the correction is applied.

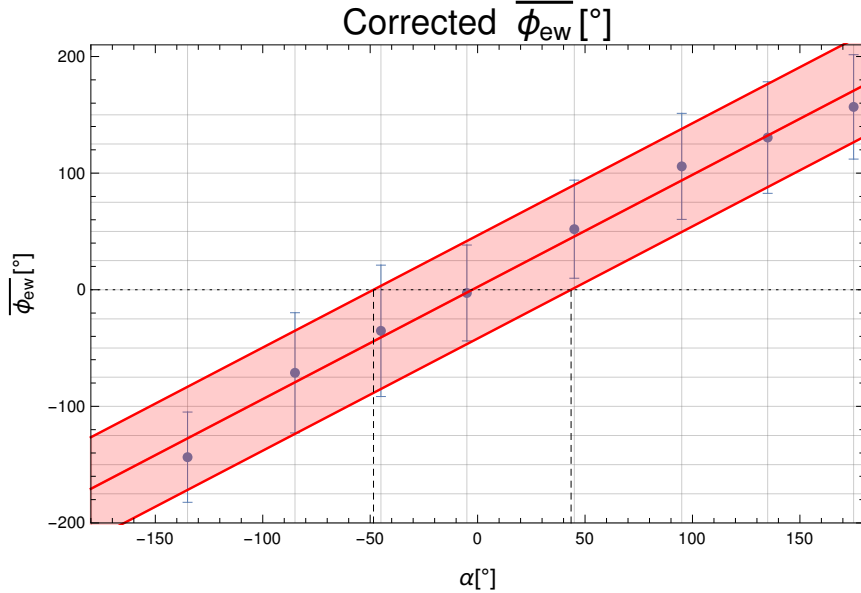


Figure 7.9: $\overline{\phi_{ew}}$ values and their corresponding α values for each of the positions defined in tab. 7.1. $\overline{\phi_{ew}} = 0^\circ$ points in the direction of channel 0. The error bar of each data point is the width σ of the Gaussian fit of the ϕ_{ew} distribution (example shown in fig. 7.8). The red line shows a linear fit. The slope is $n = (0.96 \pm 0.04)$, in agreement with the assumption of $\overline{\phi_{ew}} = \alpha$. The red band indicates the mean of all σ values, $\bar{\sigma} = 46^\circ$. If an event has a mean azimuth angle of e.g. $\overline{\phi_{ew}} = 0^\circ$, shown by the horizontal dotted line, the 1σ confidence interval for α is between -48° and 44° , indicated by the vertical dashed lines.

by measuring the voltage at the single channels using the dip switches. Additionally, the normalization using the values of $\overline{J_{i,\text{av}}^{\text{C-0}}}$ was new in this work. This also leads to an improvement on the results in [10], even if the correct numbering is applied.

In fig. 7.10, for all events of one position, the event-independent mean angle $\overline{\phi_{ew}}$ is shown in a polar plot that represents the PCB. One can see a very good agreement between these positions and the actual positions given in fig. 7.3. Thus, the chosen time cuts are in good agreement with the actual position of the particle in the scintillator box.

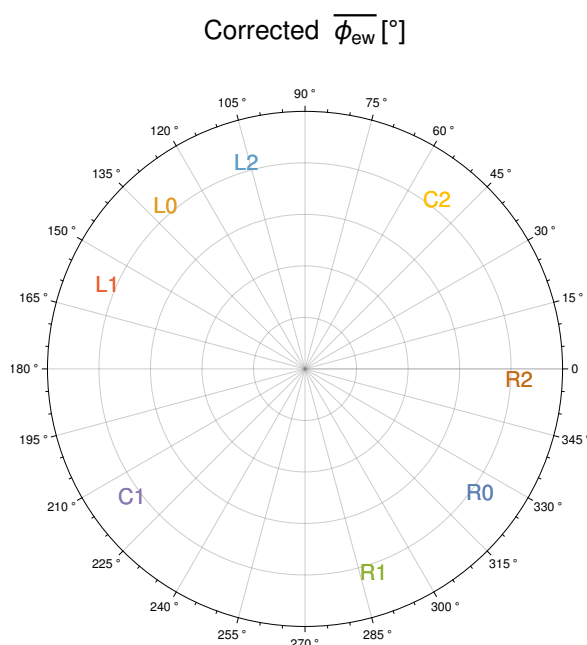


Figure 7.10: Polar plot of the event-independent mean angle $\overline{\phi_{ew}}$ of each position, indicated by the corresponding letter-number-combination. 0° points towards the corner of the box.

8 Summary and outlook

This work was written in the context of the Search for Hidden Particles (SHiP) experiment. The SHiP experiment is a proposed intensity frontier experiment to be implemented at CERN SPS. As SHiP is planned to be a zero-background experiment, background events have to be tagged and suppressed. One important component of this process is the Surrounding Background Tagger (SBT). It surrounds the experiment's decay volume and is used to tag background muons and deep inelastic scattering of neutrinos. The SBT will consist of multiple single cells filled with liquid scintillator, equipped with wavelength-shifting optical modules (WOMs) that are viewed by printed circuit boards (PCBs) equipped with silicon photo-multipliers (SiPMs). The WOMs are located inside of PMMA vessels to ensure an air gap between their walls and the liquid scintillator.

By calibrating in a dedicated setup it was found that the S14160-3050HS SiPMs have a higher gain than the S13360-3075PE SiPMs. This is in accordance with the values given in their respective datasheets.

The WOMs are used to collect light and guide it towards the PCB. This happens via total reflection inside the walls. In this work, it was tested whether the light yield of WOMs can be increased by gluing a reflector ring made of highly reflective mylar foil to the end of the tube. This would increase the efficiency of the SBT. For the PCBs using the S13360-3075PE SiPMs, no difference in light yield could be measured after the gluing of the reflector. The PCB equipped with the S14160-3050HS SiPMs registered an increase in light yield of about 14%. As these results contradict each other, the study is inconclusive. However, the effect of a reflector on the light yield can not be bigger than $\approx 15\%$.

To study whether total reflection at the end of the WOM is important for the light yield, black foil instead of a reflector was glued to the WOM tube. The light yield with black foil is about 30% lower than without black foil. Therefore, total reflection at the end of the WOM tube is an important effect for the

light yield, even without a dedicated reflector.

Further studies are needed to clarify the effect of a reflector on the light yield of a WOM tube with a SiPM array readout. However, this study found an upper limit of 15% on the improvement in light yield, which likely makes it unattractive for the SBT to attach a reflector to WOM tubes, due to a low cost-use and time-use ratio. The main source of systematic variation is the application of new optical gel. This should be studied further to get more reproducible results. A readout by adiabatic lightguides that were glued to the end of the WOM tubes was studied in [28], but it yielded a lower photon yield and lower efficiency than the readout by a SiPM array.

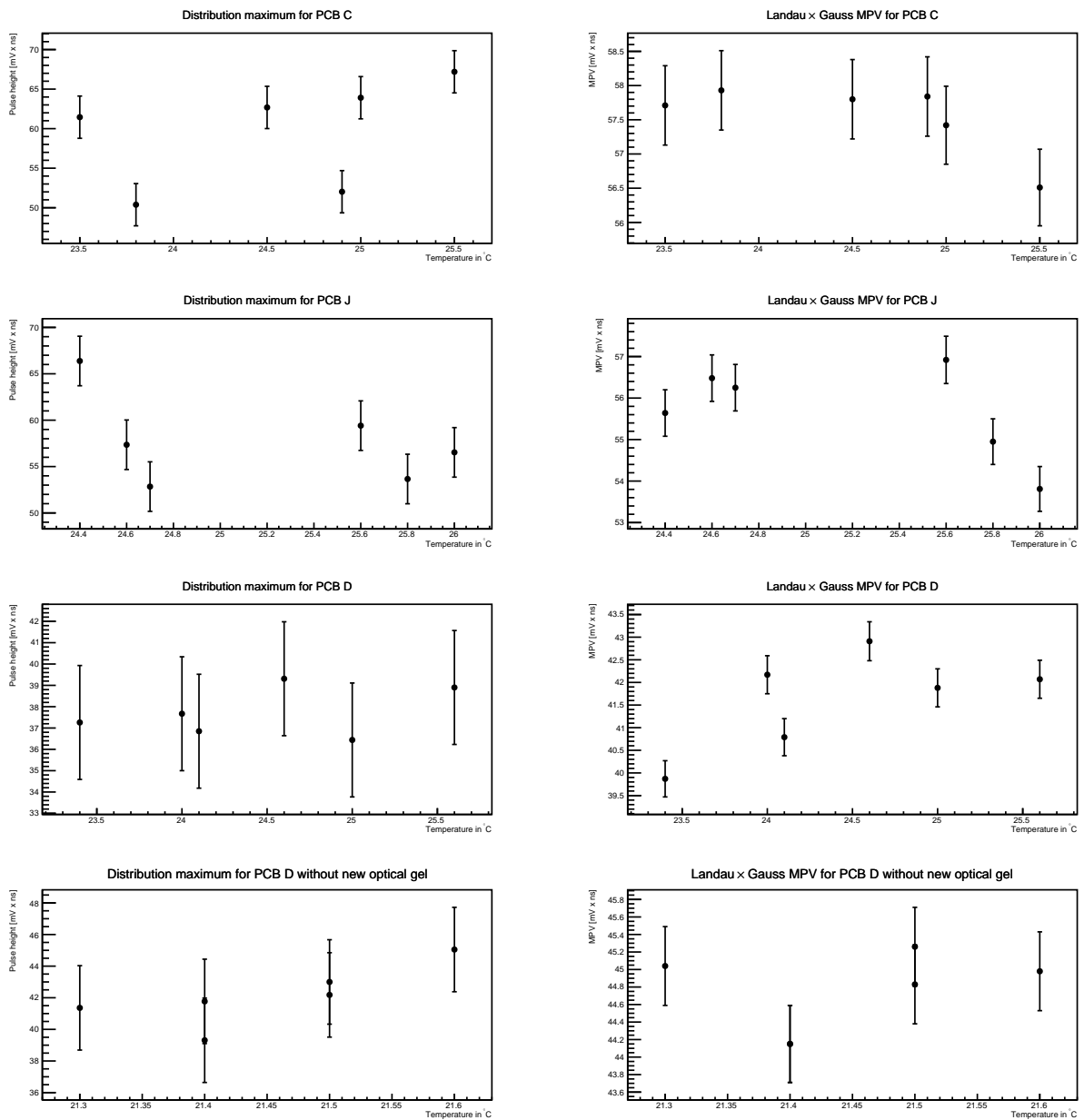
Based on a study in [10], the positional response of a PCB was investigated. The two PS above and below the liquid scintillator box which are being viewed by two photo-multiplier tubes (PMTs) each serve as a trigger for a measurement and provide information on the path a charged particle took through the box: on the one hand the PS can be moved, so that their position gives information and additionally, the difference in arrival time of the light in the PMTs can be used to gain information about the incidence location of a charged particle in the plastic scintillator. For this, one can simply divide the difference in arrival time by the speed of light in the PS. This yields the position of the crossing particle with respect to the centre of the PS. Nine incidence positions were defined, corresponding to three positions of the PS and three time cut intervals. Each position was assigned an angle α . For the position where the PS are in a central position and the time cuts only select events in the centre of the PS, called C0, one only takes particles into account that crossed the box in the location of the WOM. This means that in theory, one would expect a uniform distribution of azimuth angles. In reality, a bias in the azimuth angles was found. To account for this, the light yield of all other positions were normalised channel-wise using the light yield of the C0 position. This is an improvement on the analysis done in [10].

Each channel of the PCB got assigned an angle φ in steps of 45° . For the incidence angle of one event measured by the PCB, ϕ_{ew} , the angles of the channels φ were added as a polar sum weighted by the normalised light yield in the corresponding channel. For one run, the distribution of all ϕ_{ew} values was fitted with a Gaussian to determine the event-independent $\overline{\phi_{ew}}$ -value indicating where most of the light came from during the run. Several

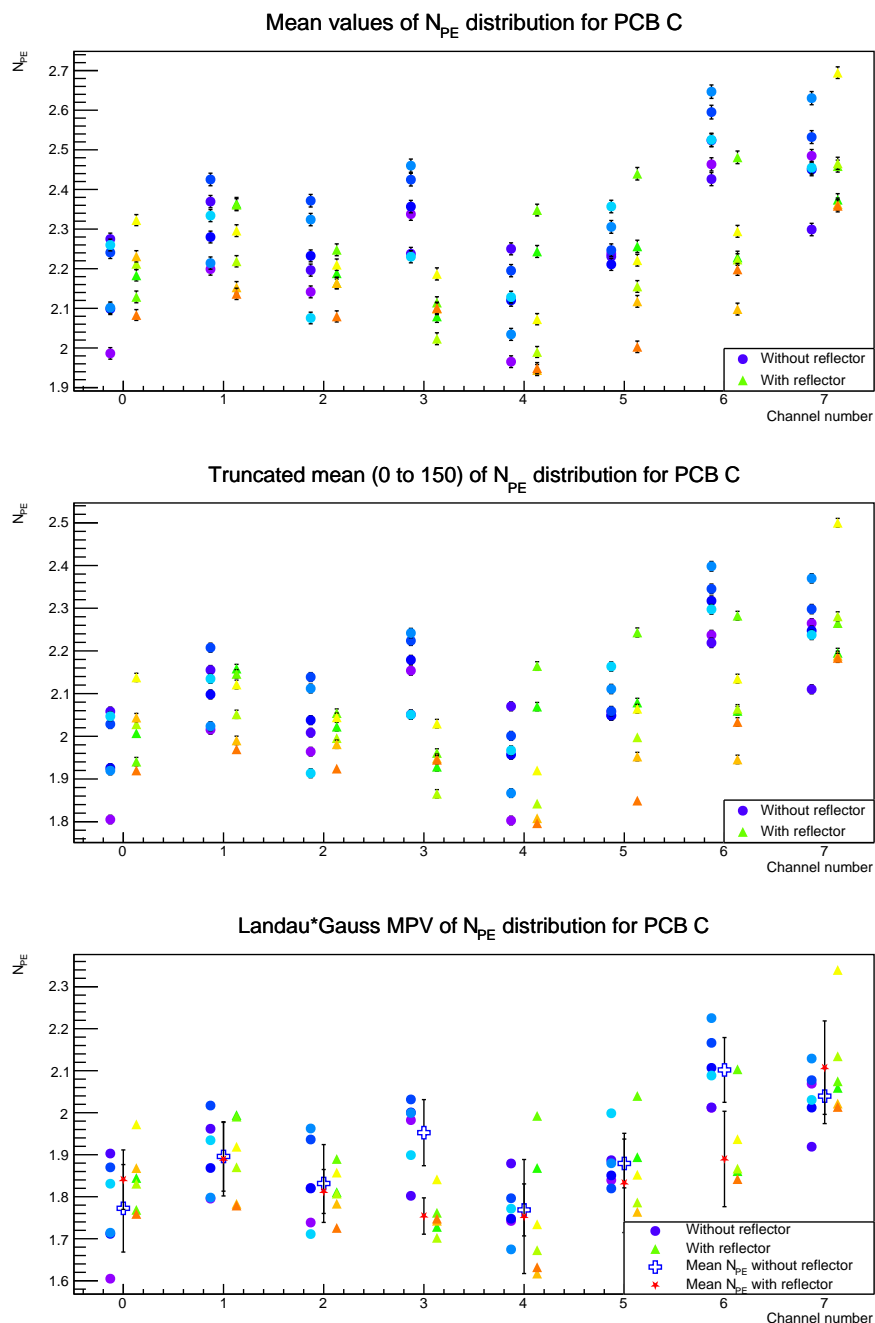
runs with different PS positions were recorded for [10].

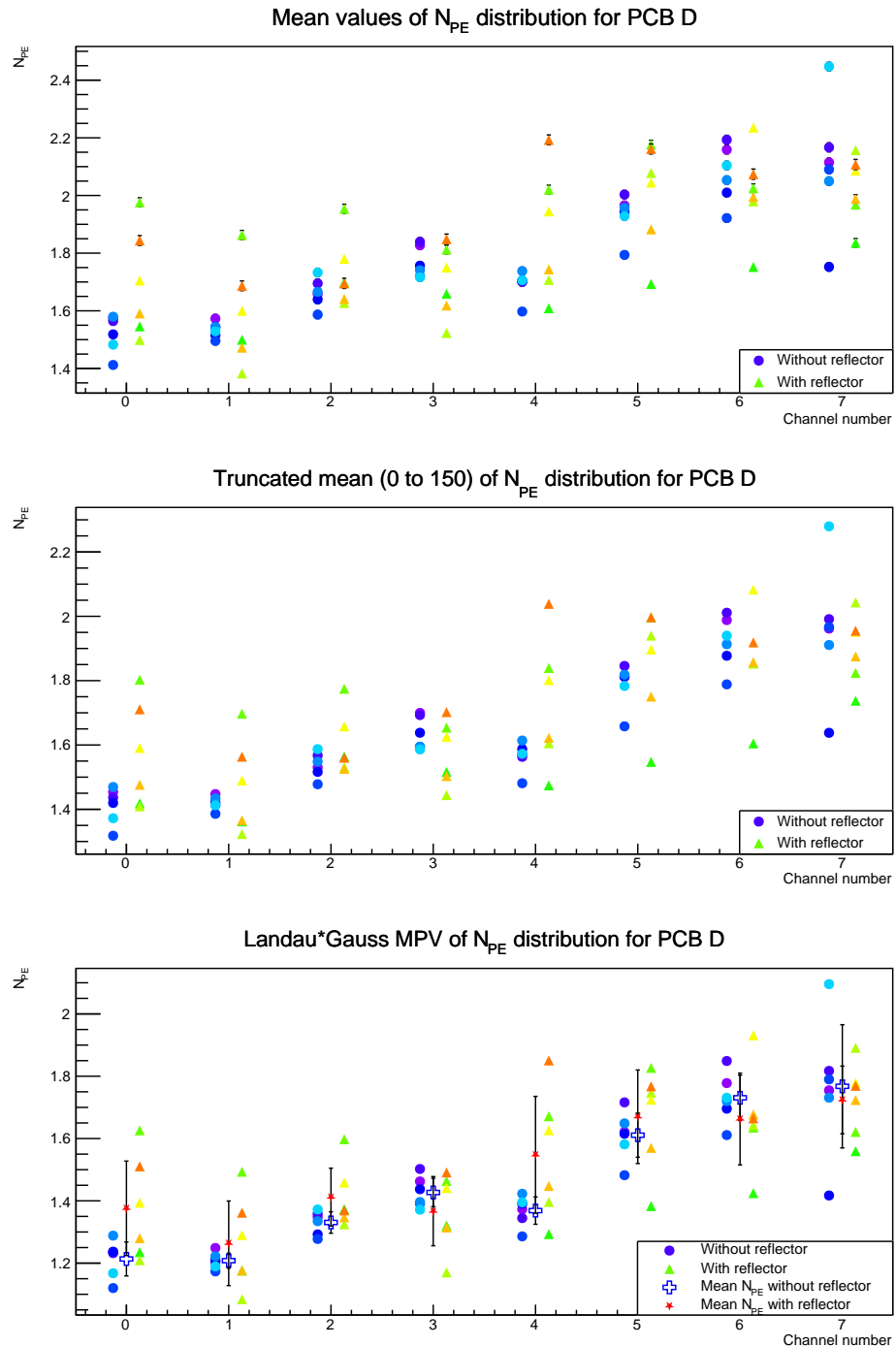
A linear correlation was found between the α and $\overline{\phi_{ew}}$ values. This means that the mean incidence angle derived from the PCB data allows a conclusion about the incidence position of a particle in the liquid scintillator. For a single event, one can make a statement about on which side of the PCB the particle crossed the liquid scintillator box at a 2σ level.

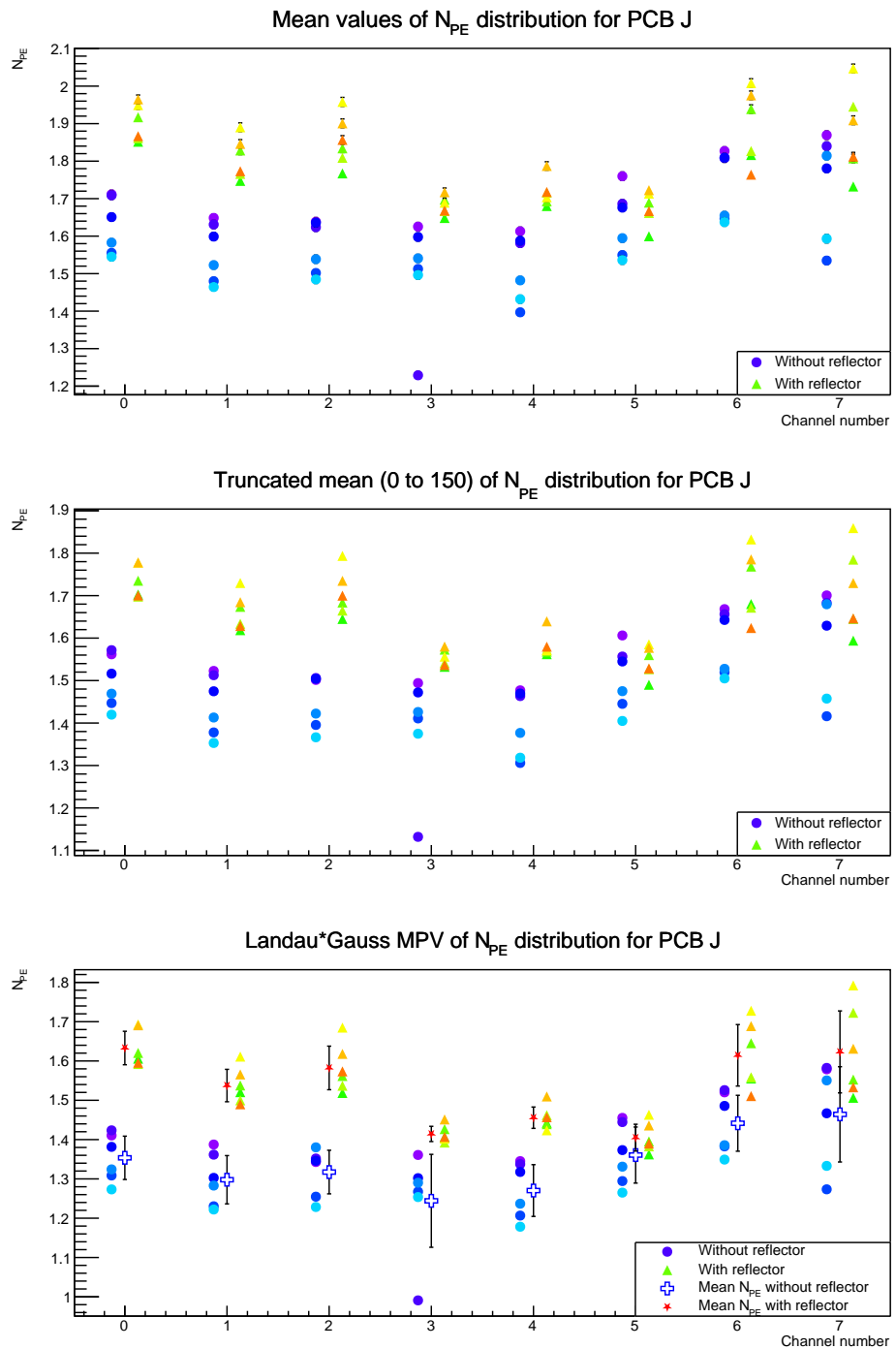
A Temperature dependence



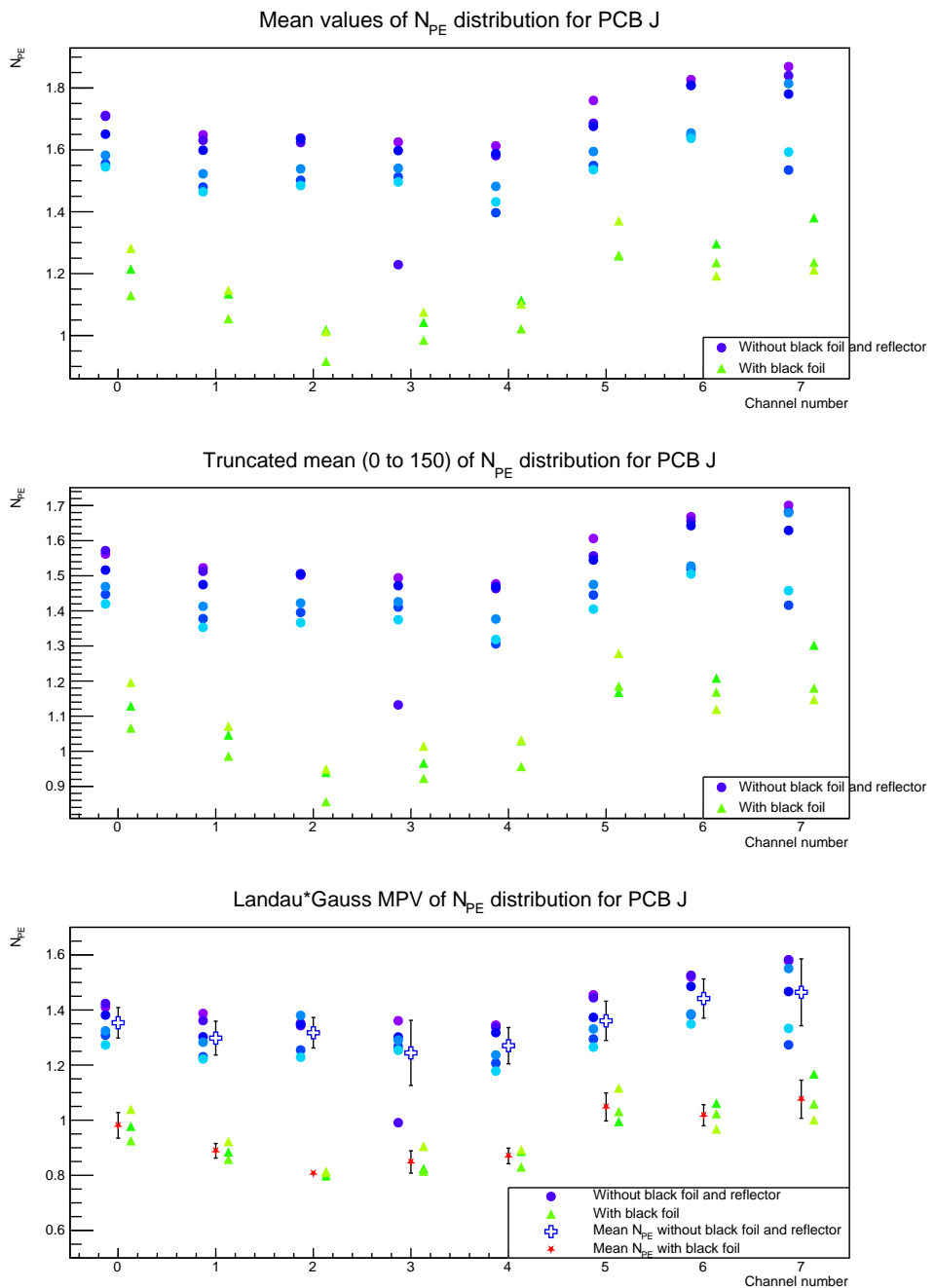
B Light yield comparison with and without reflector



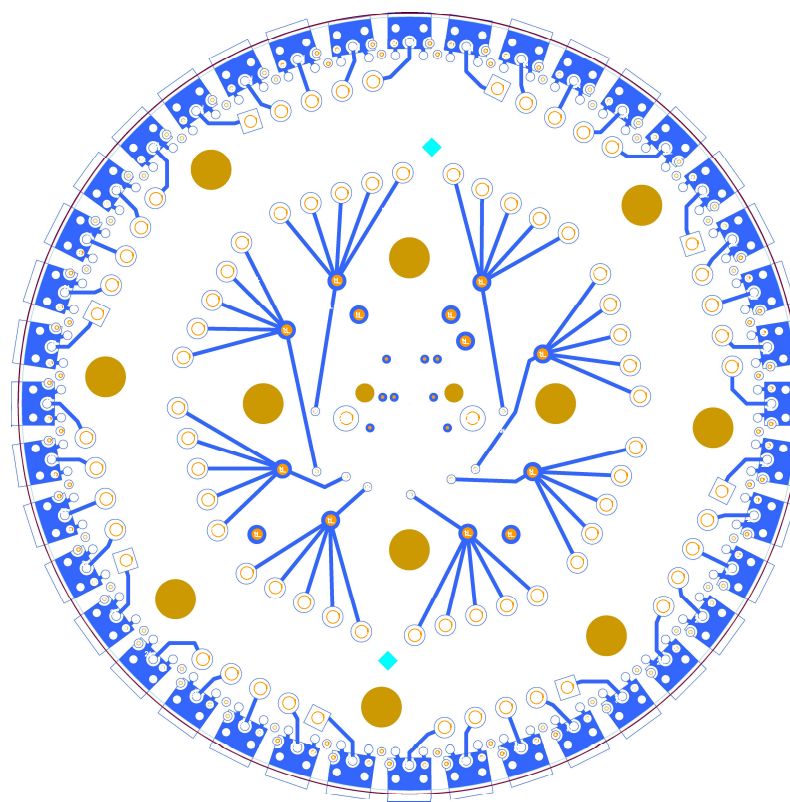




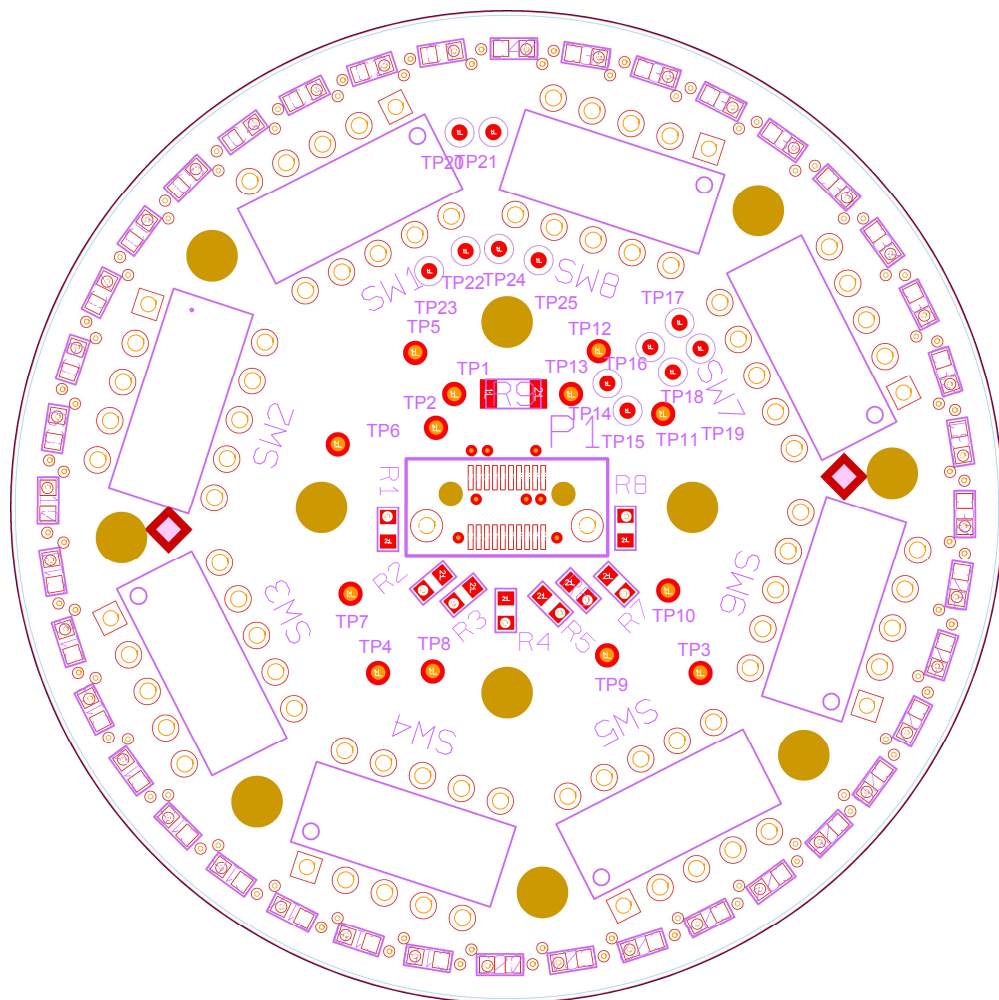
C Light yield comparison with and without black foil



D PCB design



\iP (nicht freigegeben - Teil von Gerold)\User\SIPM_PCB_HEGGEN\Mentor_SIPM_PCB\V11\PCB\SIPM_PCI



\iP (nicht freigegeben - Teil von Gerold)\User\SIPM_PCB_HEGGEN\Mentor_SIPM_PCB\V11\PCB\SIPM_PCI

Bibliography

- [1] AlFiPa. *Einsatzgebiete für Aluminium- & Verbundfolien*. Last accessed on 25.05.2022. URL: <https://alfipa.de/anwendungen/>.
- [2] Askins, M. et al. "Theia: an advanced optical neutrino detector". In: *The European Physical Journal C* 80.5 (May 2020). DOI: [10.1140/epjc/s10052-020-7977-8](https://doi.org/10.1140/epjc/s10052-020-7977-8). URL: <https://doi.org/10.1140/epjc/s10052-020-7977-8>.
- [3] Bayerlein, Dr. Reimund and Fleck, Prof. Dr. Ivor. *Characterization of a Silicon-Photomultiplier Using Ultra-Fast Pulsed LED*. Last accessed on 17.05.2022. URL: https://www.hep.physik.uni-siegen.de/teaching/masterlab/manuals/SiPM_Manual.pdf.
- [4] Bertrand, Guillaume H. V., Hamel, Matthieu, and Sguerra, Fabien. "Current Status on Plastic Scintillators Modification". In: *Chemistry - A European Journal* (20 2014). DOI: [10.1002/chem.201404093](https://doi.org/10.1002/chem.201404093).
- [5] Cova, S. et al. "Avalanche photodiodes and quenching circuits for single-photon detection". In: *Appl. Opt.* 35.12 (Apr. 1996), pp. 1956–1976. DOI: [10.1364/AO.35.001956](https://doi.org/10.1364/AO.35.001956). URL: <http://opg.optica.org/ao/abstract.cfm?URI=ao-35-12-1956>.
- [6] D'Ambrosio, C. *A short overview on Scintillators*. Last accessed on 04.03.2022. Apr. 2005. URL: https://ph-dep-dt2.web.cern.ch/CAT2005_3a.pdf.
- [7] Daya Bay and JUNO collaborations. "Optimization of the JUNO liquid scintillator composition using a Daya Bay antineutrino detector". In: *Nuclear Instruments and Methods in Physics Research Section A: Accelerators, Spectrometers, Detectors and Associated Equipment* 988 (Feb. 2021). DOI: [10.48550/ARXIV.2007.00314](https://arxiv.org/abs/2007.00314). URL: <https://arxiv.org/abs/2007.00314>.
- [8] Ehlert, Maximilian. "Zeitauflösungsuntersuchungen eines Flüssigszintillatordetektors unter Verwendung von wellenlängenschiebenden optischen Modulen". MA thesis. Humboldt Universität zu Berlin, 2020. URL: https://box.hu-berlin.de/d/cf200cbd160b45b4bcc8/files/?p=%2FMasterarbeit_MaximilianEhlert.pdf.

- [9] Ehlert, Maximilian et al. "Proof-of-principle measurements with a liquid-scintillator detector using wavelength-shifting optical modules". In: *Journal of Instrumentation* 14.03 (Mar. 2019). ISSN: 1748-0221. DOI: [10.1088/1748-0221/14/03/p03021](https://doi.org/10.1088/1748-0221/14/03/p03021).
- [10] Ernst, Andrea. "Study of the position-dependent detector response of a liquid- scintillator detector instrumented with WOMs and SiPMs using cosmic muons". BA thesis. Humboldt Universität zu Berlin, Sept. 2021. URL: https://box.hu-berlin.de/d/47ab56646cc745819549/files/?p=%2FBA_ernst_final_nomar.pdf.
- [11] Fermilab. *A Plan for Discovery*. 2011. URL: https://www.fnal.gov/directorate/plan_for_discovery/pdfs/Plan_for_Discovery_20111201.pdf.
- [12] Gutierrez, R. M. et al. "The silicon photomultiplier as a metasystem with designed electronics as metadevice for a new receiver-emitter in visible light communications". In: *SPIE Proceedings* (Sept. 2015). Ed. by Engheta, Nader, Noginov, Mikhail A., and Zheludev, Nikolay I. ISSN: 0277-786X. DOI: [10.1117/12.2190161](https://doi.org/10.1117/12.2190161). URL: <http://dx.doi.org/10.1117/12.2190161>.
- [13] Hamamatsu. *Datasheet for S13360-3075PE*. Last accessed on 19.03.2022. URL: https://www.hamamatsu.com/content/dam/hamamatsu-photonics/sites/documents/99_SALES_LIBRARY/ssd/s13360_series_kapd1052e.pdf.
- [14] Hamamatsu. *Datasheet for S14160-3050HS*. Last accessed on 19.03.2022. URL: https://www.hamamatsu.com/content/dam/hamamatsu-photonics/sites/documents/99_SALES_LIBRARY/ssd/s14160_s14161_series_kapd1064e.pdf.
- [15] Hamamatsu. *Structure of a SiPM*. Accessed on 02.03.2022. URL: https://www.hamamatsu.com/eu/en/product/optical-sensors/mppc/what-is_mppc.html.
- [16] Hanel, Joscha. "Determination of directional information from scintillation photons using SiPM-array-instrumented wavelength-shifting optical modules". BA thesis. Humboldt Universität zu Berlin, 2020.
- [17] Hollnagel, Annika. *The SHiP Experiment - Current Status and Test Beam Results*. Accessed on 15.03.2022. 2022. URL: <https://web.physik.rwth-aachen.de/~hebbeker/dpg/hollnagel.pdf>.

- [18] Kern GmbH. *Brechungsindex von Kunststoffen und Vergleichsproben*. Last accessed on 18.03.2022. 2022. URL: <https://www.kern.de/de/kunststofflexikon/brechungsindex>.
- [19] Kim, Chanho et al. "A Review of Inorganic Scintillation Crystals for Extreme Environments". In: *Crystals* (Nov. 2021). URL: <https://www.mdpi.com/2073-4352/11/6/669>.
- [20] Kirnehkrib. *Structure of an APD*. Accessed on 01.03.2022. Dec. 2011. URL: https://commons.wikimedia.org/wiki/File:APD3_German.png.
- [21] Kondylis, Konstantinos, Yannopoulou, Nikolitsa, and Zimourtopoulos, Petros. "A Study of End-Fed Arrays with Application to Single Driving-Point Self-Standing Linear Arrays". In: *FunkTechnikPlus* (4 May 2014). arXiv: [1002.3871 \[physics.class-ph\]](https://arxiv.org/abs/1002.3871).
- [22] Laboratoire de l'accélérateur linéaire. *WaveCatcher Documentation*. last accessed on 11.02.2022. URL: <owncloud.lal.in2p3.fr/index.php/s/56e4a2c53a991-cb08f73d03f1ce58ba2>.
- [23] LPKF. *LPKF ProtoMat H100 Fully Automated for High-Performance Rapid PCB Prototyping*. Last accessed on 25.05.2022. URL: <https://www.lpkfusa.com/datasheets/prototyping/h100.pdf>.
- [24] Nakamura, Yuki et al. "Characterization of SiPM Optical Crosstalk and Its Dependence on the Protection-Window Thickness". In: *Proceedings of the 5th International Workshop on New Photon-Detectors (PD18)* (Apr. 2019). DOI: [10.7566/JPSCP.27.011003](https://doi.org/10.7566/JPSCP.27.011003).
- [25] Schliwinski, Julian. "Application of Silicon Photomultiplier Arrays for the Readout of a Liquid-Scintillator Detector using Wavelength-Shifting Optical Modules". MA thesis. Humboldt Universität zu Berlin, Dec. 2019. URL: https://box.hu-berlin.de/d/cf200cbd160b45b4bcc8/files/?p=%2Fmt_final_21_12_19_J_Schliwinski.pdf.
- [26] Schulte, Lukas et al. *A large-area single photon sensor employing wavelength-shifting and light-guiding technology*. June 2013. arXiv: [1307.6713 \[astro-ph.IM\]](https://arxiv.org/abs/1307.6713).
- [27] Scientifica. *eMUSIC MiniBoard User Guide*. Second Version, Revision 2.5a. Feb. 2019. URL: http://siub.ub.edu/down/music/emusic-miniboard.user_guide.r2.5a.pdf.

-
- [28] Shihora, Linus. "Test and Comparison of Two Liquid Scintillator Detector Prototypes with WOM-Readout in Terms of Efficiency and Detector Response". MA thesis. Humboldt Universität zu Berlin, Oct. 2019. URL: https://box.hu-berlin.de/d/cf200cbd160b45b4bcc8/files/?p=%2Fthesis_L_shihora.pdf.
 - [29] SHiP Collaboration. *A Facility to Search for Hidden Particles (SHiP) at the CERN SPS*. Technical Proposal (CERN-SPSC-2015-016, SPSC-P-350). Apr. 2015. URL: <https://arxiv.org/pdf/1504.04956.pdf>.
 - [30] SHiP Collaboration. *SHiP Experiment - Progress Report*. (CERN-SPSC-2019-010, SPSC-SR-248). Jan. 2019. URL: <https://cds.cern.ch/record/2654870>.
 - [31] Zacharias, Max. "Efficiency measurement of a transparency-improved liquid-scintillator detector with SiPM-WOM readout". BA thesis. Humboldt Universität zu Berlin, Dec. 2020. URL: <https://box.hu-berlin.de/d/da5ae2dabad74a92ad25/files/?p=%2FBachelorarbeit%2FBachelorarbeit.pdf>.
 - [32] Zimmermann, Jan. "Efficiency studies of a liquid-scintillator detector based on wavelengthshifting optical modules". MA thesis. Humboldt Universität zu Berlin, Oct. 2020. URL: https://box.hu-berlin.de/d/cf200cbd160b45b4bcc8/files/?p=%2FMasterarbeit_Zimmerman.pdf.

Eidesstattliche Erklärung

Ich, Alexander VAGTS, bestätige, dass diese Masterarbeit mit dem Titel „Improvement of light yield and spatial resolution of a liquid-scintillator detector equipped with a wavelength-shifting optical module coupled to a SiPM array“ und die darin präsentierte Arbeit von mir verfasst und erarbeitet wurde. Die verwendeten Quellen wurden vollständig angegeben.

Unterschrift:

Datum und Ort:
